Enzymatic Degradation of Carbon Nanotubes and Mechanical Separation of Carbon Nanocups

by

James A. Gaugler II

B.S., University of Pittsburgh, 2012

Submitted to the Graduate Faculty of the

Kenneth P. Dietrich School of Arts and Science in partial fulfillment

of the requirements for the degree of

Master of Science

University of Pittsburgh

2016

UNIVERSITY OF PITTSBURGH

KENNETH P. DIETRICH SCHOOL OF ARTS AND SCIENCE

This thesis was presented

by

James A. Gaugler II

It was defended on

November 30th, 2015

and approved by

Dr. Jill Millstone, Assistant Professor, Chemistry

Dr. Renã A. S. Robinson, Assistant Professor, Chemistry

Committee Chair: Dr. Alexander Star, Professor, Chemistry

Enzymatic Degradation of Carbon Nanotubes and

Mechanical Separation of Carbon Nanocups

James A. Gaugler II, M.S.

University of Pittsburgh, 2016

In this work, single-walled carbon nanotubes and nitrogen-doped multi-walled carbon nanotubes are introduced and studied in the contexts of biodegradation and drug delivery, respectively. Single-walled carbon nanotubes have been shown to degrade in the myeloperoxidase enzyme system, and in Chapter 2, the mitigating effects of antioxidants and polyethylene glycol coating on nanotube biodegradation are examined. In Chapter 3, a simple method for the separation of nitrogen-doped multi-walled carbon nanotubes by grinding in a mortar and pestle is reported.

TABLE OF CONTENTS

LIST OF TABLES

LIST OF FIGURES

LIST OF EQUATIONS

LIST OF COMMONLY USED ABBREVIATIONS

CNT: carbon nanotube

DOS: density of states

SWCNT: single-walled carbon nanotube

MWCNT: multi-walled carbon nanotube

N-MWCNT: nitrogen-doped multi-walled carbon nanotube

o-SWCNT: oxidized single-walled carbon nanotube

CVD: chemical vapor deposition

DOF: degree of freedom

RBM: radial breathing mode

TEM: transmission electron microscopy

MPO: myeloperoxidase

NCNC: nitrogen-doped carbon nanocup

PEG: polyethylene glycol

AFM: atomic force microscopy

XPS: X-ray photoelectron spectroscopy

AA: ascorbic acid

GSH: glutathione

PREFACE

This thesis is submitted to the graduate faculty of the Kenneth P. Dietrich School of Arts and Science in partial fulfillment of the requirements for the degree of Master of Science in Chemistry. It contains my research results from 2012 to the present day, and a summary of the work of others.

My time at the University has been an absolutely amazing experience, in which I have had the great privilege of learning from so many brilliant minds. I owe my progress in life to many people. I thank my advisor, Dr. Star, for his patience and open-mind. I truly appreciate the freedom to learn and insightful advice that you have provided over the years. I also thank my lab-mates for their constant willingness to help and listen and for the countless fascinating conversations about life and science. Among my lab-mates, a special thanks is owed to Gregg Kotchey for his patience and kindness in training me as an undergraduate. Lastly, I thank my family and loved ones, whose love, support, and encouragement provide the foundation upon which I pursue my aspirations in science.

1.0 Introduction

The carbon nanotube, an allotrope of carbon first reported in 1952[1], was propelled into the spotlight by Sumio Iijima's work in 1991.[2] This one-dimensional allotrope is characterized by its record-breaking aspect ratio[3] and tensile strength[4], along with extremely high electrical conductivity.[5] The outstanding properties of carbon nanotubes (CNTs) have triggered an intense, world-wide research effort and promise advances in applied materials science. In the laboratory setting, CNTs have excelled in a diverse range of applications[6–8] and may eventually attain widespread commercialization. However, before commercialization, the risks of accidental or intentional CNT exposure to biological systems must be assessed.[9] Here, both sides of the science will be explored. In Part 2, the fate of CNTs in a biological system will be explored *in vitro* using the myeloperoxidase enzyme system as a model for *in vivo* mammalian biodegradation. In Part 3, a method for the separation nitrogen-doped carbon nanocups (NCNCs) with potential applications in drug delivery is reported.

1.1 Structure and Properties of Carbon Nanotubes

Carbon nanotubes are best understood in relation to graphene, which is commonly regarded as the model system for sp^2 hybridized carbon nanomaterials[10], so a brief review of graphene's structure and electronic properties is warranted. Graphene, is a planar, two-dimensional, hexagonal lattice of sp^2 hybridized carbon atoms (Figure 1a) with the remarkable property of being a zero-band gap semiconductor exhibiting ballistic conduction and a massless Dirac electron.[11] The behavior of the delocalized electrons in the π-molecular orbital gives rise to these unique electronic properties, and is modeled by the dispersion relation (Figure 1b).

The dispersion relation, which describes the distribution of electronic states allowed within a primitive unit cell, is derived from the constraints of the first Brillouin zone, itself defined by the reciprocal lattice. The real and reciprocal lattice of graphene along with the first Brillouin zone are shown in Figure 1c. The transformation from a real to reciprocal lattice vector is described in Equation 1, where $\boldsymbol{a}_i$ is a real lattice vector, $\boldsymbol{b}_i$, is the reciprocal lattice vector, and δ_{ij} is the Kronecker delta.

$$\boldsymbol{b_i} = \frac{2\pi\delta_{ij}}{\boldsymbol{a_i}} \tag{1}$$

The reciprocal lattice is a convenient form for modeling the interaction between wave and lattice while preserving information on the connectivity of real lattice points. From the reciprocal lattice, one can define its unit cell, known as the Brillouin zone, the boundaries of which confine the range of allowed wavevectors within the lattice. The relationship between the real lattice and the maximum allowed value of the wavevector is defined by Equation 2, where k_{BZ} represents the maximum wavevector, and a represents a primitive lattice translation vector. Furthermore, the Brillouin zone may be translated according to Bloch's theorem to model a periodic graphene crystal of arbitrary size.

$$k_{BZ} = \frac{\pi}{a} \tag{2}$$

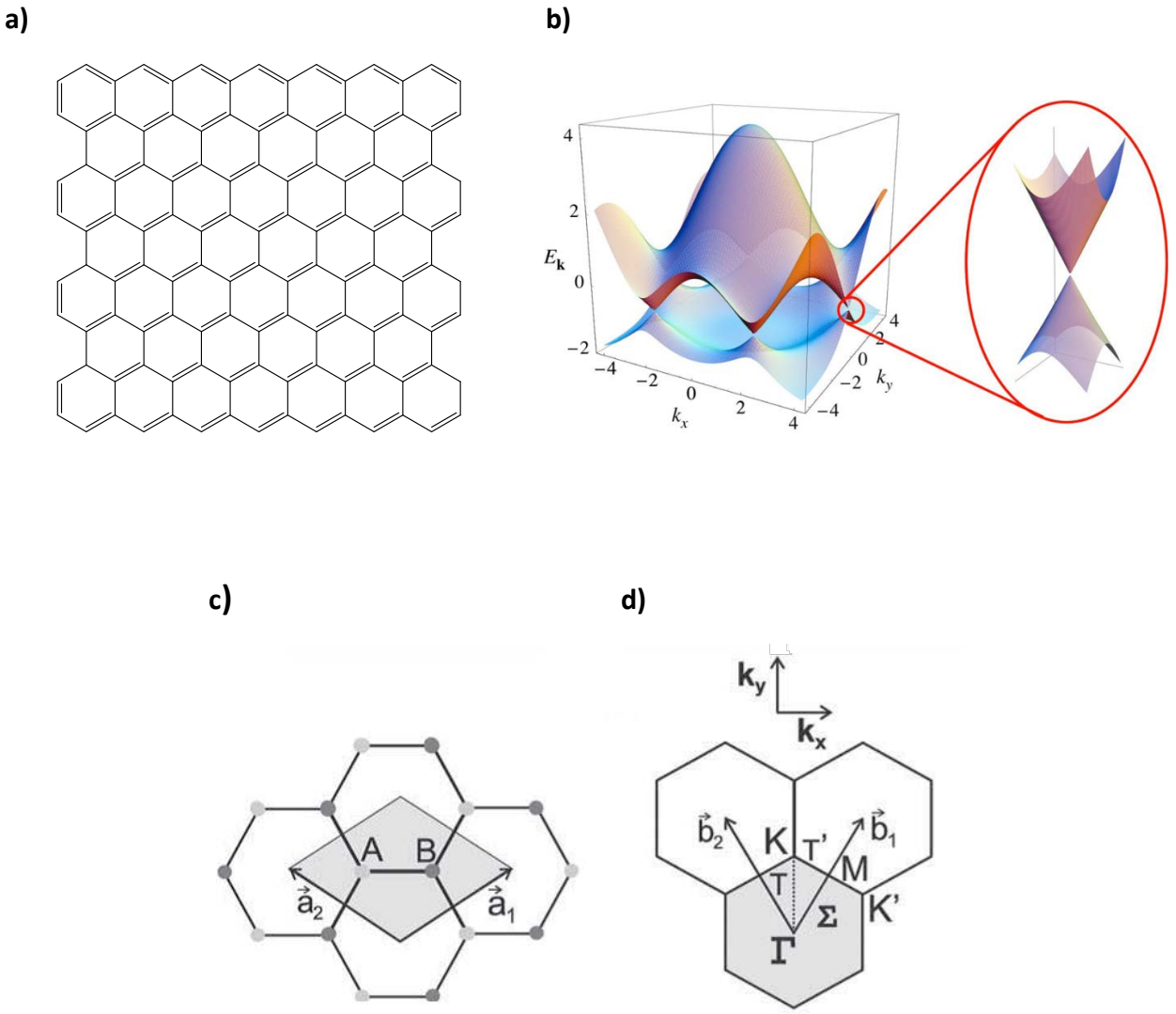

Figure 1: a) Bond-line representation of a single layer H-terminated graphene sheet. b) Graphene's dispersion relation. Inset shows Dirac cone. Adapted from reference 81. c) Real graphene lattice, showing the two unique carbons, A and B, along with the primitive unit cell defined by translation vectors a_1 and a_2. d) Reciprocal graphene lattice with unit cell defined by reciprocal lattice vectors b_1 and b_2. The first Brillouin zone, with high symmetry points K, M, Γ and K′, is shaded gray. Adapted from reference 12.

In physical terms, graphene's dispersion relation is a plot of electron energy against the wavevectors, k_x and k_y, which describes, in this case, the momentum of π-orbital electrons in graphene's x and y dimensions. The positive E values correspond to graphene's delocalized conduction band and the negative values correspond to the valence band. The Fermi level, the total chemical potential of the electrons, lies between the bands at zero energy.

From the dispersion relation, it is clear that the Fermi level lies in the gap between the valence and conduction bands, which is typical of semiconductors. However, unlike most semiconductors, graphene possesses a shrinking continuum of energy states which result in the separation of the two bands by only a dimensionless point. Thus, with no true gap between the valence and conduction band, graphene is considered a zero-band gap semiconductor.[11] It is also evident that, for energy values close to zero, the momentum and energy of the electron exhibit a linear relationship which result in values of zero energy at zero momentum. This unique structure in the dispersion relation, known as a Dirac cone, describes the energy-momentum relation of massless particles such as a photon. Thus, at low energy, the π-orbital electrons behave as massless particles which can transition from the valence band to the conduction band with zero inertia.[11]

The structure of a CNT is easily derived from graphene by a simple transformation described pictorially in Figure 2 and the electronic properties are determined by the constraints imposed upon graphene's dispersion relation by the symmetry of a given CNT's unit cell. Since CNTs are considered one-dimensional nanomaterials, the effects of quantum confinement become significant along its circumference, and the allowed electronic states in this direction are quantized.

a) **b)**

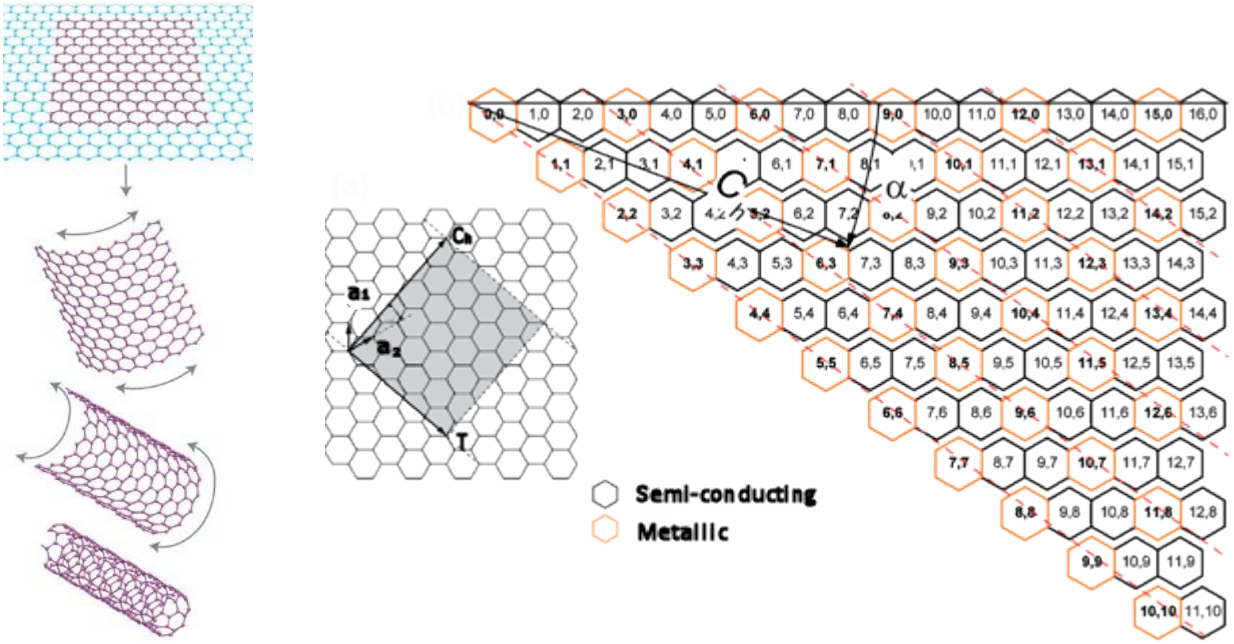

Figure 2: a) Purple section of graphene lattice is conceptually folded to form a carbon nanotube. Adapted from reference 10. b) The inset image shows translation vectors, a_1 and a_2, the roll-up vector, C_h, and the long axis of the CNT, T. The colored image displays a range of (n,m)-indices and their resultant electronic properties. Adapted from reference 73.

A CNT is formed conceptually by rolling the graphene lattice into a seamless cylinder along a vector[12] defined in Equation 3, where C_h is the chiral angle, and a_i is a primitive lattice translation vector.

$$C_h = n\boldsymbol{a_1} + m\boldsymbol{a_2} \equiv (n, m) \quad (3)$$

The chiral vector, denoted in short as the (*n,m*)-indices, determines the symmetry of the CNT's unit cell, controls edge structure, and allows for a chiral twist, in the lattice. The symmetry imparted by this vector determines whether a given CNT is semi-conducting or metallic. The effect is superficially described by Equation 4, which predicts that for a given value of (*n*,*m*), a CNT will be metallic when *k* is an integer value and semiconducting for non-integer *k* values.

$$\frac{(n-m)}{3} = k \quad (4)$$

The consequences of the roll-up vector are described in greater detail by applying "cutting lines" to graphene's dispersion relation.[13] This technique is used to derive a CNT's density of states (DOS) for a given chiral index and clearly highlights the origin of a CNT's semi-conducting or metallic nature. The cutting lines, shown around the K-point of graphene's dispersion relation in Figure 3 denote energy sub-bands within the dispersion relation for a given CNT. The number and spacing of cutting lines is derived from the number of hexagons in the CNT unit cell and the reciprocal lattice vectors of the CNT unit cell, respectively.[12]

When a cutting line intersects with the Dirac point of the dispersion relation, then the electronic states of that CNT exist as a continuum, and the CNT is metallic in character. If no cutting line crosses this point, then the CNT is a semiconductor imbued with a true band gap. Additionally, a local energy maximum, E_i, for a cutting line at wavevector, k_i, corresponds to sharp increase in the DOS, known as a van Hove singularity. These features appear in 1-D materials as a result of quantum confinement and significantly affect the material's optoelectronic properties.[14]

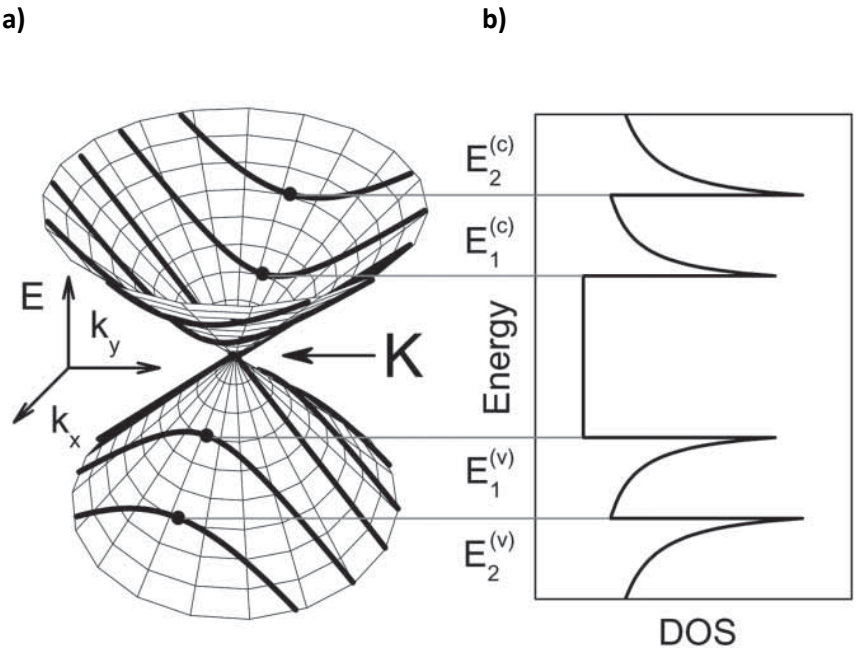

Figure 3: a) Bolded lines represent cutting lines applied to the K-point of graphene's dispersion relation. Maxima are indicated by black dots, which correspond to van Hove singularities in b) the CNT density of states (DOS) diagram. Adapted from reference 12.

The prototypical CNT is a single-walled carbon nanotube (SWCNT), however, there are many morphologically distinct CNTs. Various synthetic conditions result in multi-walled carbon nanotubes (MWCNTs) [15], oxidized-SWCNTs[16], or stacked-cup nanotubes[17], among myriad others. While an exhaustive description of all possible CNT morphologies is beyond the scope of this thesis, nitrogen-doped, stacked cup nanotubes and oxidized-SWCNTs are of particular interest in this research.

Nitrogen doping during CNT synthesis has been shown to result in a stacked-cup MWCNT morphology[18] (Figure 9). It is theorized that the trigonal pyramidal conformation adopted by trivalent nitrogen imparts curvature to the CNT lattice[18] which results in this unique morphology. The inclusion of nitrogen creates a highly disordered lattice by disrupting the periodic hexagonal structure.[19] Oxidized-SWCNTs (o-SWCNTs) represent a distinct class of carbon nanotubes because the sidewalls and edges have been imparted with a range of oxygen-containing functionalities and lattice defects by harsh oxidative conditions.[16] These functional groups impart certain desirable properties such as aqueous solubility[20] and enhanced biodegradative susceptibility.[21]

1.2 Synthesis of Carbon Nanotubes

Numerous routes exist for the synthesis of CNTs. After the discovery of CNTs as a product of electrical arc discharge[2], CNTs were soon synthesized by laser ablation[22] and chemical vapor deposition[23] (CVD), among other approaches. Laser ablation, while invaluable in the early stages of CNT research, has fallen in popularity due to high cost.[24] The remaining methods, an optimized arc discharge process and CVD represent the major synthetic routes due to a balance of yield, cost, and morphological control.[24,25]

Arc discharge synthesis is a conceptually simple process, schematically outlined in Figure 4a, in which a large current is passed through a carbon electrode which partially vaporizes by resistive heating and carbon nanotubes are formed in the resultant high energy environment. The growth mechanism of CNTs in this environment is a complex issue and the subject of ongoing debate, with studies encompassing all phases of matter present within the chamber, along with the effect of the electric field.[26] As this is the oldest technique for the synthesis of CNTs, a wide array of modifications have been made to the core concept. In varying the composition of the electrode, the current passed through the electrode, and the composition and pressure of gas within the discharge chamber, myriad approaches have been designed to tailor the yield for CNTs for yield, specific chirality, or morphology.[27]

The synthesis of CNTs by CVD, outlined in Figure 4b, encompasses many unique precursors and methods, all of which incorporate high effective temperatures and a metal catalyst. In a typical CVD synthesis, a carbon-containing molecule is fed into the reactor as a gas, decomposed on a catalyst by high temperature, pressure or plasma, and deposited as a thermally stable sp^2 hybridized carbon lattice.[27] The resultant CNT morphology and growth mechanisms of this process are highly dependent on the carbon source, the choice of metal catalyst, catalyst substrate, and the temperature of the reactor.[27]

a) **b)**

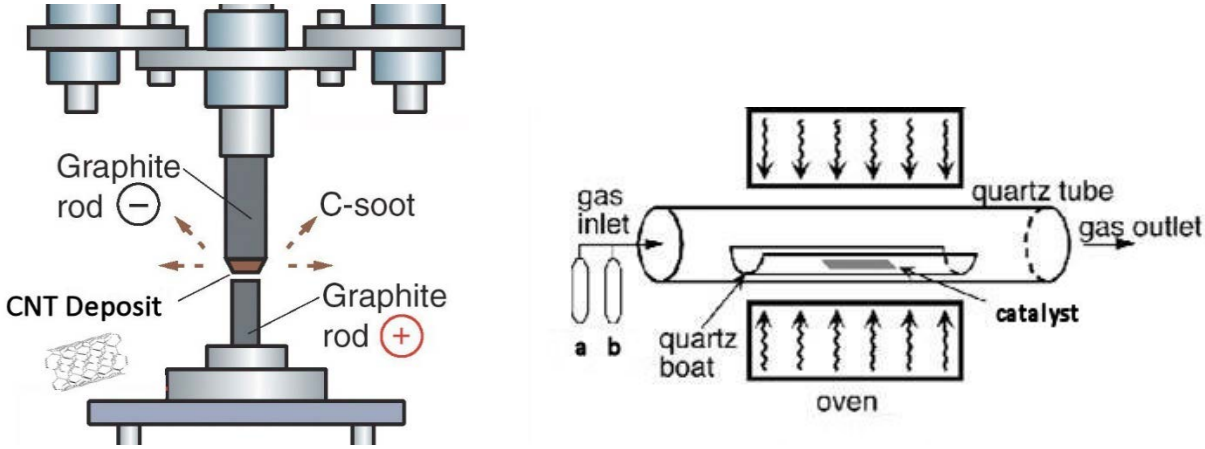

Figure 4: a) Schematic of arc discharge device indicating graphite cathode and anode. Adapted from reference 74. b) Schematic of CVD apparatus, gas tanks labeled "a" and "b" refer to in the carbon feedstock and an inert carrier gas, respectively. Adapted from H. Kind at École polytechnique fédérale de Lausanne.

Two basic approaches exist in the introduction of a metal catalyst to the CVD chamber. One approach sees the catalyst pre-formed upon a substrate and placed in the chamber prior to CNT growth. The approach affords the highest degree of control over catalyst diameter and, in turn, CNT diameter.[28] However, this control comes at the expense of yield, since only a flat, 2-D surface is available for growth. The alternative approach uses a "floating catalyst", which makes use of the CVD chamber's full volume by allowing CNT synthesis to occur in the vapor phase.[27] In this process, a vaporized catalyst precursor, such as ferrocene, and carbon feedstock are simultaneously introduced to the chamber, with catalyst particle formation occurring *in situ* by thermal decomposition.[29] This process allows a continuous introduction of catalyst and can afford high yields at the expense of reduced control over catalyst diameter.

The choice of carbon source and any accompanying feed gases are a critical factor affecting CNT morphology.[27] Depending on the strength of the interaction between catalyst and carbon source, departures from the single-walled nanotube morphology, such as multi-walled or stacked-cup CNTs may be observed.[30] For example, multi-walled, stacked-cup CNTs shown can result from the inclusion of a nitrogen source (Figure 9) or in the case of strong interaction between the carbon source and catalyst.

1.3 Characterization of Carbon Nanotubes

1.3.1 UV-vis spectroscopy

UV-vis spectroscopy reveals information on the electronic structure of CNTs by detecting the absorption of light by a sample. In UV and visible spectrum, light is absorbed by an electron which causes it to transition to a discrete higher energy level. A planar sp^2 carbon lattice presents a broad, featureless absorption spectra, as a result of its smooth DOS function.[31] However, as discussed earlier, the 1-D confinements of a cylindrical sp^2 lattice imbue a CNT's DOS with sharp discontinuities known as van Hove singularities.[12] Depicted in Figure 5, electrons may transition between symmetric singularities, however transitions between dissimilar energy bands forbidden by selection rules.[32] Since the exact energy and number of van Hove singularities is determined by a CNT's chiral index, the distribution of chiralities within a mixture can be analyzed by UV-vis spectroscopy. Furthermore, using this technique, a CNT sample can be characterized as metallic, semiconducting, or a mixture of both. This technique is valuable in that it allows a range of CNTs to be probed, reporting on all CNTs present within a sample.[33]

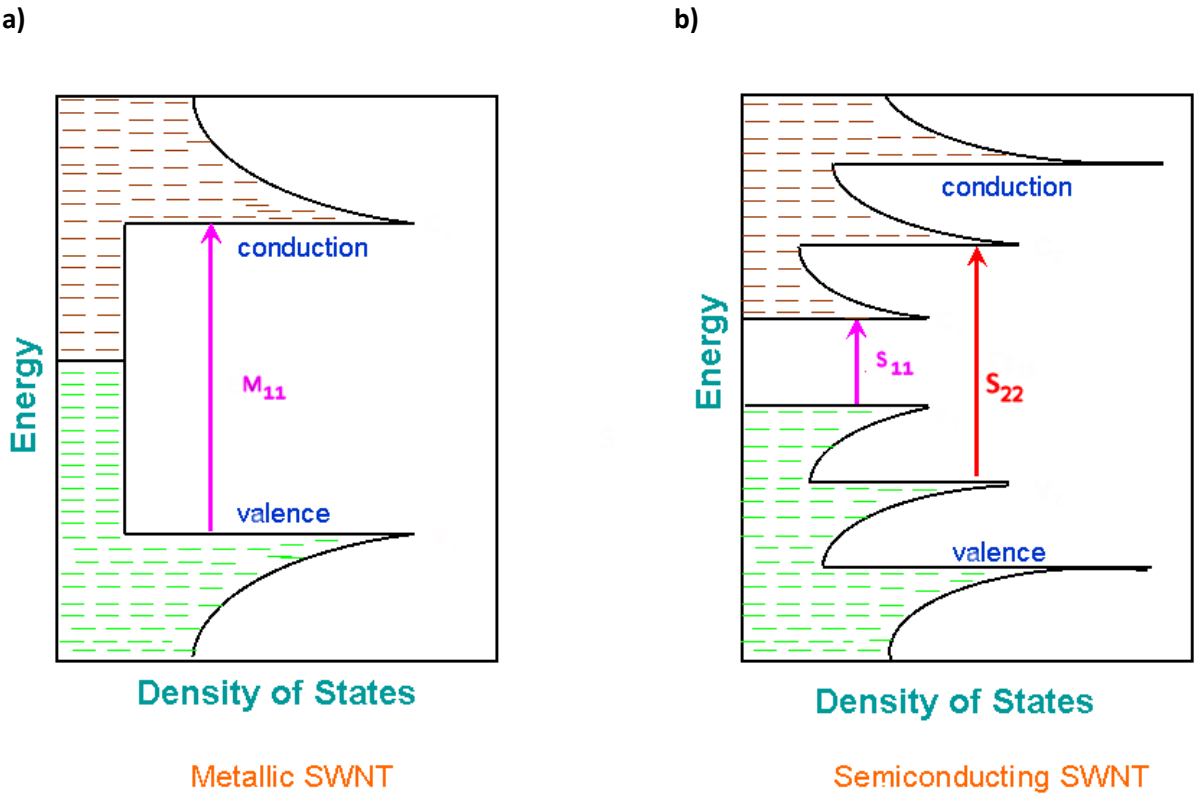

Figure 5: Density of states diagram from a) metallic and b) semiconducting SWCNT. Electronic excitation is shown for the first van Hove singularity, M_{11} for the metallic-SWCNT. Excitations of the first and second van Hove singularities are shown for the semiconducting SWCNT. Adapted *via* Wikimedia Commons from Materialscientist.

1.3.2 Raman Spectroscopy

Raman spectroscopy has risen to prominence in the field of carbon nanomaterials, as it provides highly detailed structural and electronic information. This technique is uniquely suited for the identification and characterization of sp^2 carbon allotropes because each allotrope displays a unique and easily distinguishable set of Raman signals[12], shown in Figure 6a, from which simple conclusions regarding the material's structure can be drawn.

Raman spectroscopy is the study of light scattered inelastically by an illuminated material. The vast majority of incident photons are scattered elastically by Rayleigh scattering, however, approximately one in 10 million are scattered by an inelastic process known as Raman scattering.[34] This phenomena occurs only when a compound's electron density can be polarized by incident light and when this polarization can couple to some internal degree of freedom (DOF), generally, a vibrational or phonon mode.[12] This coupling between a compound's polarized electric field and atomic vibration creates a condition in which the energy of the polarized field can increase or decrease by vibrational coupling. The loss or gain of energy by this process results in an emitted photon with an energy differing from the incident photon, which is observed as inelastically scattered light. Inelastically scattered light is divided into two categories, Stokes and anti-Stokes. In Stokes scattering, the scattered photon loses energy, and conversely, an anti-Stokes photon gains a quanta of energy. A general representation of these phenomena is outlined schematically by the Jablonski diagram shown in Figure 6b.

In Stokes scattering, the oscillating electric field of an impinging photon polarizes a compound's electron density and excites the compound to a virtual electronic state, which couples to and excites some ground-state vibrational mode, thus imparting a quanta of energy to the vibrational system. Since the time scale of virtual state relaxation is significantly shorter than vibrational relaxation, this quanta of energy remains in the vibrational system upon relaxation of the virtual state, and a red-shifted photon is

emitted. In the case of anti-Stokes scattering, the incident photon finds the compound in a vibrationally excited state upon excitation to a virtual state. Due to coupling between the two states, the virtual state relaxes completely to the ground electronic and vibrational state, and a scattered photon is emitted with an energy greater than the incident photon by a value equal to the energy of the excited vibrational state. This phenomenon is observed as the emission of a blue-shifted photon, and is significantly more rare than Stokes scattering as an excited state is generally less populated than the ground state at thermodynamic equilibrium. Together, these two processes result in peaks shifted in wavelength from the elastically scattered Rayleigh line. This shift, known as the Raman shift, is independent of the incident light's wavelength, and the source of structural and chemical information gleaned from a substrate.

Raman scattering in CNTs is a resonant process, meaning a signal is only observed for CNTs which possess a bandgap equal to the exciting laser energy.[35] CNTs exhibit several Raman-active phonon modes, each of which report on a distinct structural component. The most commonly observed modes result in the G-band and D-band, where "G" refers to graphitic and "D" refers to defect. The G-band arises from the collective tangential movement of carbon atoms in the sp^2 lattice (Figure 6c), creating a Stokes shift of 1500-1600 cm^{-1}. The D-band, at 1350 cm^{-1}, originates from symmetry-breaking defects or boundaries in the carbon lattice which activate a forbidden mode.[12] Throughout the literature, the ratio of the intensity or area of these two Raman bands is commonly used to estimate the degree of structural perfection of the sp^2 carbon lattice.[36] The overtone of the G peak, known as the G' or 2D peak, is useful in estimating the number of layers in stacked graphitic carbon. This band will show a single peak in a single-layer lattice, becoming split and irregular with an increased number of layers.[37] The D and G bands, along with their overtones, are common to all graphitic materials, however the radial breathing mode (RBM) is unique to CNTs. The RBM, observed at 100-300 cm^{-1}, is due to the symmetric in-phase expansion of CNT atoms in the radial direction (Figure 6d). The primary utility of this band is in estimating the diameter of CNTs, and for confirming their presence.[12] A simple expression, shown in Equation 5, allows for the

estimation of CNT diameter based on RBM, where ω_r is the Raman shift of the RBM and d is the CNT diameter in nanometers.

$$\omega_r = \frac{223.75\ cm^{-1}}{d\ (\mathrm{nm})} \tag{5}$$

a)

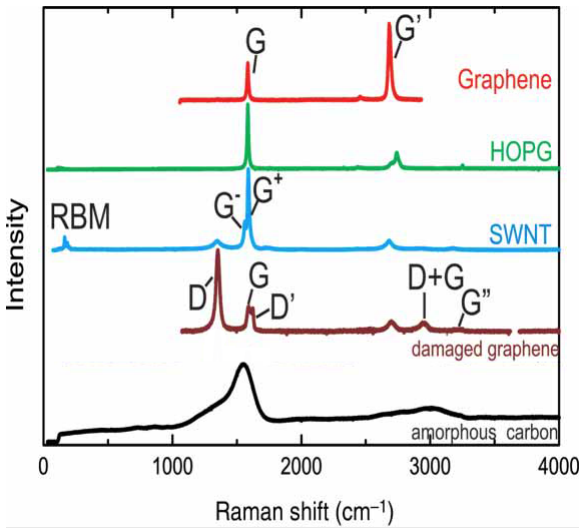

b) **c)** **d)**

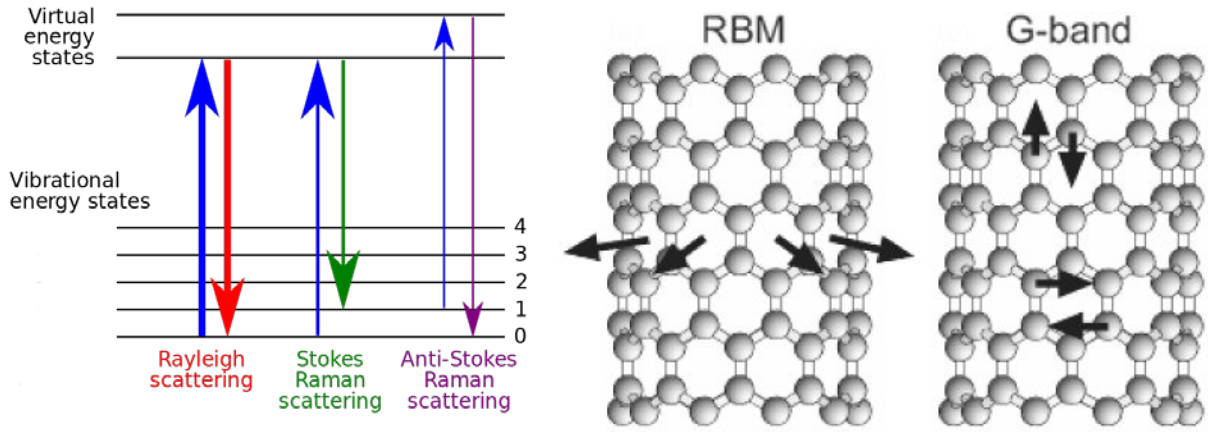

Figure 6: (a) Typical Raman spectra are shown for graphene, highly oriented pyrolytic graphite (HOPG), SWCNT, damaged graphene, and amorphous carbon. Relevant scattering bands are labeled. Adapted from reference 12. (b) Jablonski diagram showing excitation (blue arrows) and relaxation (colored arrows) for Rayleigh and Raman scattering events. Adapted *via* Wikimedia Commons from Moxfyre. (c) Arrows indicate motion of carbon atoms in radial breathing phonon mode. (d) Tangential motion of carbon atoms in G-band phonon mode. Adapted from reference 82.

1.3.3 Transmission Electron Microscopy

Transmission electron microscopy (TEM), a staple of materials science, allowed for the first observation of CNTs in 1952.[1] Conceptually, TEM is a simple imaging technique, not entirely dissimilar from light microscopy. Depicted in Figure 7, a high energy electron beam is emitted from a cathode filament, electromagnetically focused, and passed through the sample to be detected on a phosphor screen or charge coupled device (CCD). As electrons pass through the sample, the repulsive forces of the sample's electron cloud cause the beam electrons to experience scattering. The phenomena of electron scattering can be divided into distinct regimes defined, in part, by the angle and direction of scattering. Specific imaging techniques are required to detect each distinct type of scattering. Here, bright-field imaging, which detects electrons scattered at relatively small angles upon passing through the sample, will be discussed.

Forward-scattered electrons deviating from the beam at angles < 3° fall under the bright-field regime, in which the extent of scattering depends on the thickness, density, atomic number and crystallinity of the material.[39] Areas of greater thickness and density intuitively result in increased scattering, as the atomic radius and number of atoms present in a given area directly relate to the probability of a scattering event. Similarly, the scattering probability increases with atomic number, (Z), scaling in magnitude roughly by (Z^2).[38] Scattering within a crystalline sample, while complex, can be understood in analogy to the classic single-slit experiment with light. If the electron beam is aligned with the lattice spacing of a crystalline material, an electron passing through the sample will behave similary to light passing through a single slit. Just as a light wave scatters and spreads out upon exiting the slit, an electron will show a similar scattering profile. In this case, since electrons are well aligned with the "slit" they incur a small scattering probability and most electrons will exit the "slit" with minimal scattering on average. Conversely, in areas where the lattice is not aligned with the electron beam or the sample is amorphous, a greater degree of scattering will be observed.

In bright-field imaging, electrons scattered at a high angle are not detected as they do not reach the imaging device, thus reduced image intensity is observed in regions of high density, thickness, or low crystallinity. This scattering creates the bright-field mage, so-called as the void spaces exhibit the highest image intensity.

The maximum resolution of TEM is governed by the effective wavelength of the electron. Features separated by a distance below approximately half the wavelength cannot be resolved. This limit, known as the diffraction limit, is described by Equation 6,

$$d = \frac{\lambda}{2NA} \tag{6}$$

where *d* is the size of the maximum distance between features, λ is the wavelength of the electron and NA is the numerical aperture of the system. The wavelength of the electron, as with all matter, is determined by its energy. Thus the energy of the electron beam is a crucial factor in determining maximum resolution. The relationship between electron energy and wavelength is described by the de Broglie relation given by Equation 7 for the specific case of an electron.

$$\lambda = \frac{h}{\sqrt{2m_0E\left(1+\frac{E}{2m_0c^2}\right)}} \tag{7}$$

Here, *E* is the electron's energy, m_0 is the electron's rest mass, *h* is Planck's constant, and *c* is the speed of light. For an electron energy of 80 keV, the corresponding wavelength is 4.33 picometers. In theory, this value would allow for sub-atomic resolution, but distortions created by imperfect focusing of the electron beam result in resolutions significantly lower, typically in the single nanometer range.[39]

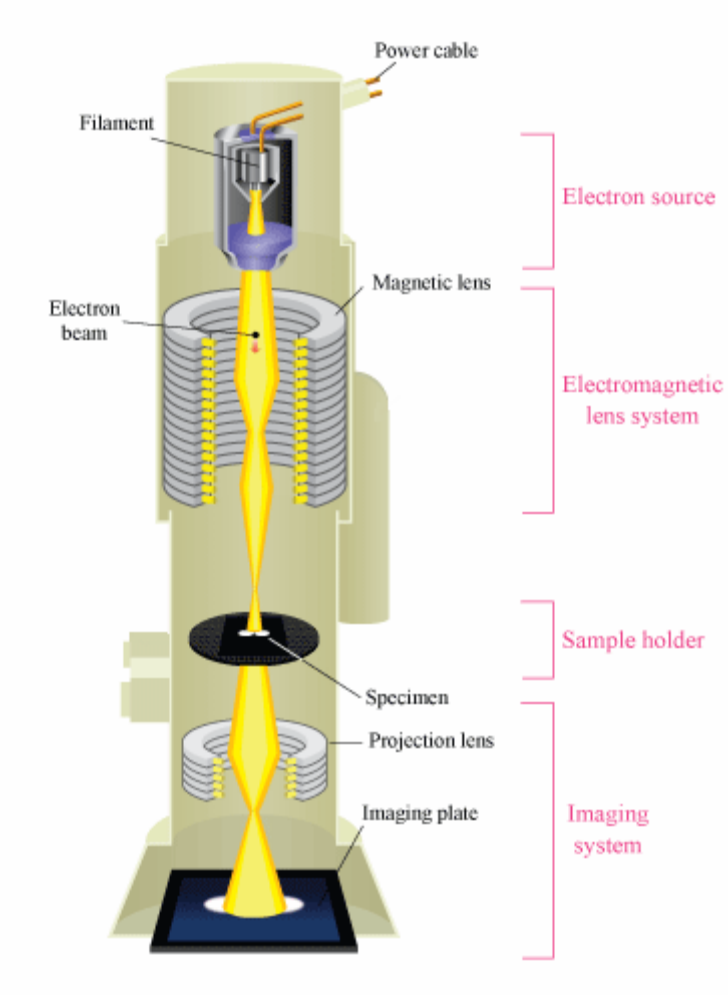

Figure 7: Schematic of transmission electron microscope. The electron beam, depicted in yellow, is shown passing through a sample. Adapted from reference 75

1.4 Carbon Nanotubes in the Myeloperoxidase System

1.4.1 Structure and Function of Myeloperoxidase

Myeloperoxidase (MPO), a 146 kDa enzyme of the peroxidase family, is an important component of the immune response to a foreign body, and thus a model system for the study of CNT biodegradation in animals. This enzyme, depicted in Figure 8a, is primarily expressed in neutrophil granulocytes, the most abundant form of white blood cells in mammals.[40] Upon exposure to a foreign body, the neutrophil undergoes a respiratory burst[41] in which MPO stored within azurophilic granules is secreted into the extracellular space.[42] Once excreted, MPO catalyzes a reaction in which H_2O_2 and Cl^- are consumed to form hypochlorous acid. It is theorized that the primary function of myeloperoxidase is the production of hypochlorous acid as a strong anti-microbial agent.[43] The high reduction potential of hypochlorous acid is the primary theoretical basis for the mechanism of CNT biodegradation.[44]

Structurally, MPO is a cationic homodimer, consisting of two identical, functionally independent 73 kDa monomers connected by a cysteine bridge. Each monomer is composed of a glycosylated 15-kDa light chain, and a 58-kDa heavy chain. The light chain possesses the modified iron protoporphyrin IX active site. This heme group is located within a deep crevice which only allows for the diffusion of small molecules (*e.g.* H_2O_2 and Cl^-) to the iron atom.[43] However, a hydrophobic pocket exists near the heme cavity to which CNTs may bind[43] and experience enhanced degradation due to the high local HOCl concentration or exposure to reactive intermediates of the peroxidase cycle.[44]

Hypochlorous acid is synthesized by MPO at the heme site through the peroxidase cycle, in which H_2O_2 and a chloride anion are principle components.[43] The process (Figure 8b) has H_2O_2 oxidize the heme Fe^{+3} to form Compound 1, an oxy-ferryl species ($Fe^{+4} = O$) with a porphyrin π-radical cation. This complex can then react with chloride to form the hypochlorite ion, (OCl^-), while reducing iron(IV) to its original

oxidation state and completing the cycle. The hypochlorite ion, a weak base, exists in equilibrium with its conjugate acid, HOCl, as it diffuses from the heme site to serve as a powerful oxidant.

1.4.2 Mechanism of Carbon Nanotube Biodegradation by Myeloperoxidase

HOCl is proposed as the primary oxidant for CNTs in this system due to its high reduction potential.[45] While HOCl can reach the CNT diffusion, it is also possible that CNTs may bind to a hydrophobic pocket near the heme group, thus facilitating enhanced degradation.[44] The possible CNT binding sites and docking simulations are shown in Figure 8. In addition to HOCl, a range of reactive intermediates produced by MPO[46] are also theorized to participate in CNT biodegradation, however their effect is likely to be less pronounced due to their lower redox potential, of E=1.15V.

Reactive intermediates of the MPO peroxidase cycle has been proposed as a secondary CNT degradation path. The peroxidase cycle has been observed to create radical compounds in the absence of chloride by reactions between the heme site and hydroperoxides.[46] These radicals may degrade CNTs directly or react with radical supporting amino acid residues[47] near the proposed CNT docking site to indirectly create a degradative environment.

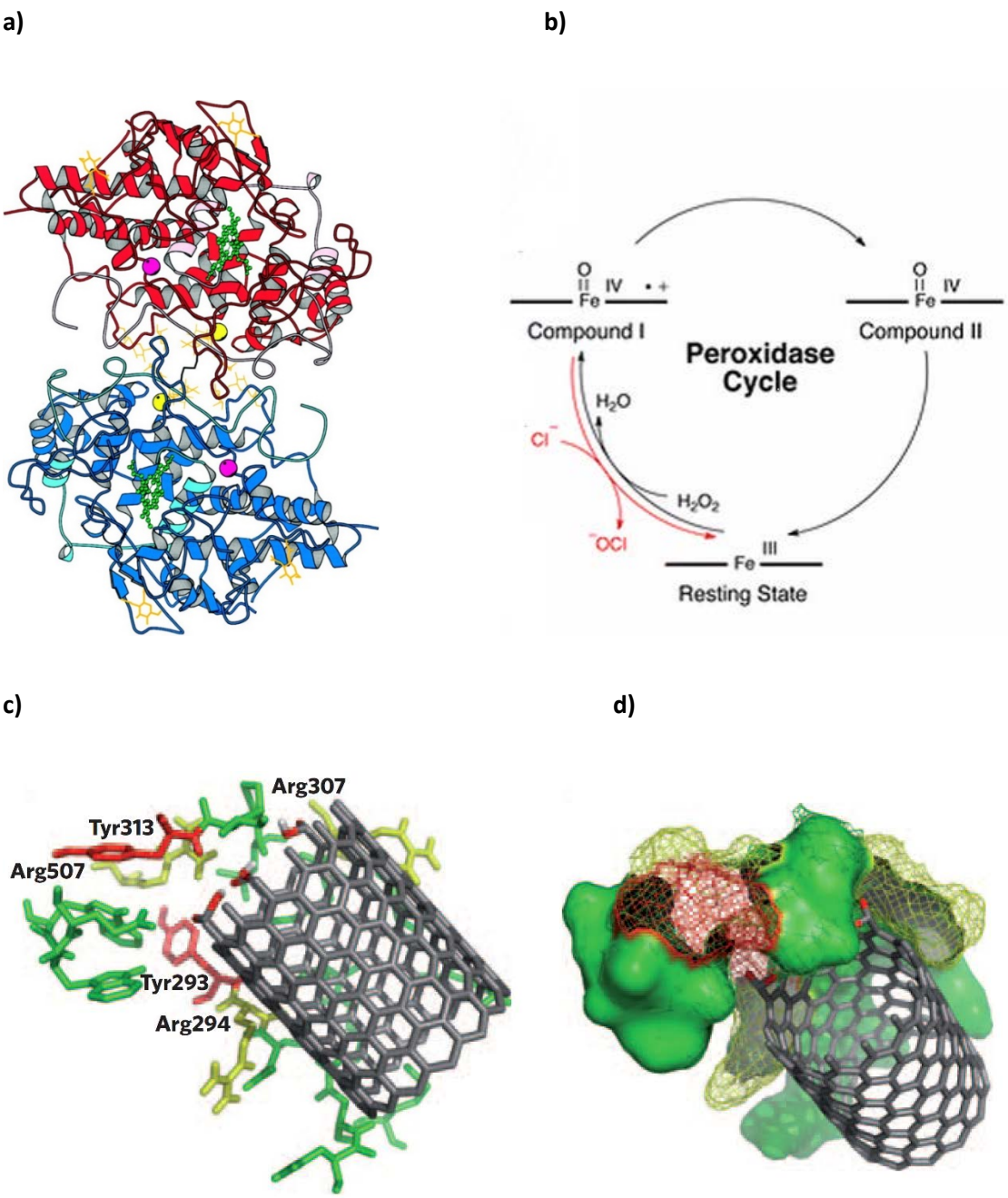

Figure 8: a) Ribbon cartoon of MPO, the heme group is visible in both monomers as a green ball-and-stick model. Adapted from reference 76. b) Peroxidase cycle of MPO demonstrating iron redox cycle and generation of hypochlorite. Adapted from reference 45. c) MPO-docking simulation showing interaction between o-SWCNT carboxyl moieties and catalytically active amino acids. D) Space filling model of preferred o-SWCNT docking site. Adapted from reference 44.

1.5 Mechanical Separation of Nitrogen-Doped Carbon Nanocups

If a CNT is synthesized with nitrogen dopants, a MWCNT morphology in which the graphitic lattice forms a series of stacked cup structures (Figure 9a) will often be formed. This repeating cup structure, called a nitrogen-doped carbon nanocup (NCNC) has been reported to be separable from the nanotube by various means such as sonication[17], ball-milling[48], or grinding by mortar and pestle. These individualized cups (Figure 9b) have been the target of research for applications in drug delivery[17] as their size and surface energy[8] allow spontaneous and passive transport across the phospholipid bilayer of the cell membrane.[49] Additionally, the cup structure may be well-suited for drug delivery as a drug payload can be trapped inside the cup by sealing the opening.[17]

a) **b)**

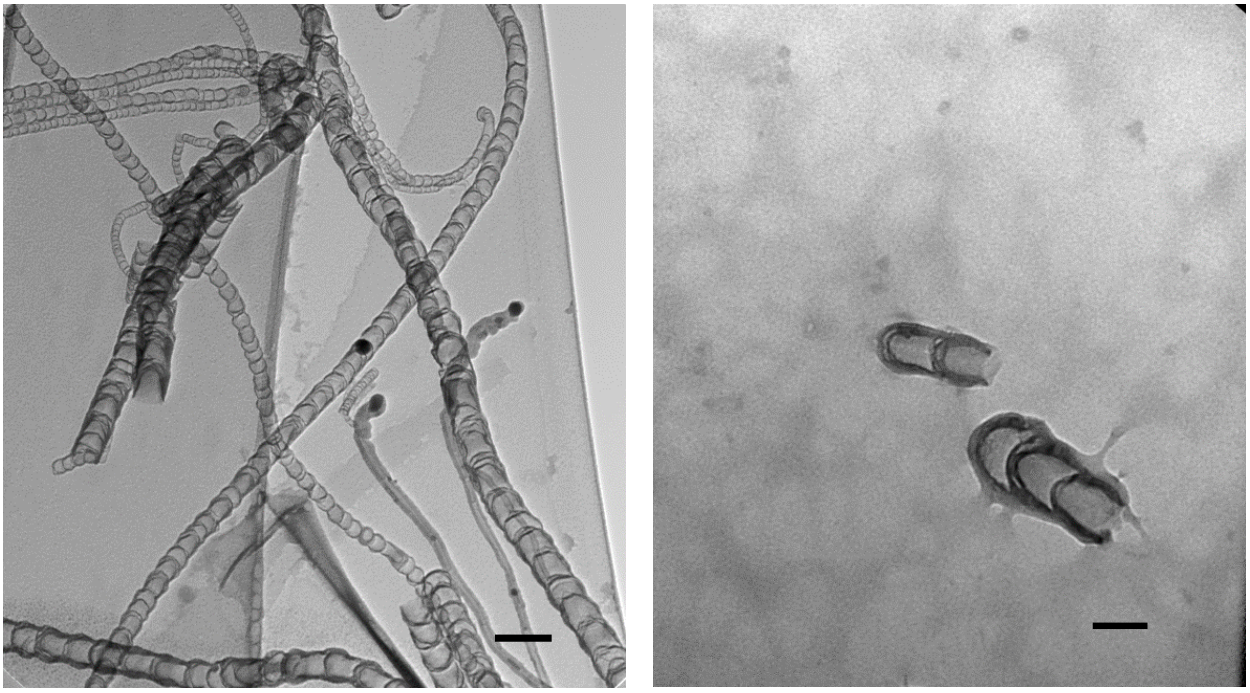

Figure 9: TEM images depicting unseparated NCNCs (a) and separated NCNCs (b) after one hour of grinding by mortar and pestle. Scale bares are 100 nm and 50 nm for (a) and (b), respectively.

2.0 Carbon Nanotube Biodegradation by Myeloperoxidase

The health and safety concerns associated with CNTs have been investigated in many fields, with harmful effects found in aquatic, terrestrial, and animal models.[50] CNTs have exhibited significant toxicity in animal models, in part, due to their rigid rod morphology and high aspect ratio, which bear similarities to asbestos.[51] The sharp needle-like CNT structure can inflict mechanical damage to cells and the high aspect ratio may be resistant to macrophage phagocytosis during the immune response to a foreign body.[52] The prolonged and futile effort of a macrophage's attempt to remove the foreign body results in a condition known as frustrated phagocytosis. The chronic inflammation and oxidative stress incurred by frustrated phagocytosis is a primary concern in assessing the biological consequences of CNT exposure.[53] A full study of the interactions between CNTs and the animal immune system will require a broad, multi-disciplinary investigation. Here, the *in vitro* myeloperoxidase (MPO) enzyme system serves as a model for the degradative process in animal phagocytosis.

In particular, the properties of CNTs and cellular components which may prevent degradation have been explored in the context of this enzyme system. The following subsection will explore the mitigating effect of the antioxidants ascorbic acid and glutathione on the MPO catalyzed degradation of o-SWCNTs. The final subsection of this chapter will explore the degradative susceptibility of polyethylene glycol functionalized o-SWCNTs within the MPO system.

2.1 Effect of Antioxidants on *in vitro* Biodegradation

This section explores the mitigating effects of the antoxidants ascorbic acid (AA) and glutathione (GSH) on the *in vitro* biodegration of o-SWCNTs by MPO. The material contained within Section 2.1 was published as a research paper[45] in the journal, *J. Mater Chem. B*.

List of Authors: G. P. Kotchey, J. A. Gaugler, A. A. Kapralov, V. E. Kagan, and A. Star.

Author Contributions: GK, VEK, and AS conceived and designed the experiments. GPK performed absorption, Raman and fluorescence spectroscopies, and transmission microscopy. AAK performed electron paramagnetic resonance spectroscopy (EPR) and fluorescence spectroscopy. JAG fabricated antioxidant treated o-SWCNTs and performed absorption spectroscopy.

2.1.1 Experimental Details

2.1.1.1 Enzymatic Degradation of o-SWCNTs

Oxidized arc discharge single-walled nanotubes (o-SWCNTs) with 1.0-3.0% carboxylic acid functionality were purchased from Carbon Solutions Inc. (P3, Riverside, CA, USA).

O-SWCNT solutions (1 mg mL^{-1}) were prepared by sonicating 1.0 mg of P3 o-SWCNTs in 1mL of 0.1M phosphate buffer with 300 µM DTPA for 1 h. Stock solutions of AA (250 mM), GSH (250 mM), H_2O_2 (18.75 mM), and NaCl (5 M) were prepared using nanopure water. As received (AR MPO) and buffer exchanged MPO (BE MPO) solutions were employed for (+) and (-) Cl^- experiments, respectively, due to the presence of trace chloride salts in the lyophilized AR MPO. AR MPO was reconstituted in 350 µL of nanopure water to a final concertation of 2.0 µM for the (+) Cl^- experiments. BE MPO was prepared by buffer exchange of AR MPO with 0.1M phosphate buffer using an Amicon Ultra 4 filter for a final volume of 350 µL. Activity of AR and BE MPO was compared by employing fluorescence-kinetics measurements

(Figure A1) using Amplex Red and the BE quantity used in experiments was adjusted to obtain equal reaction rates. Table A1 describes the experimental conditions for the degradation of SWCNTs with MPO. Each experimental condition was performed in triplicate in a 96 wellplate receptacle. An Epoch microplate spectrophotometer (BioTek, Winooski, VT, USA) recorded absorbance values at 999 nm for before the enzymatic reactions were initiated (day 0). Hourly additions of H_2O_2, AA, and GSH stock solution were made to create samples with nominal concentrations of 75 µM, 1mM, and 1mM respectively. In total, 7 additions were made on day 0 and 8 additions were made on Days 1, 2 and 3. AP MPO and BE MPO concentrations were refreshed by adding 4.0 µL and 4.8 µL, respectively, on days 1, 2, and 3. Samples were kept in an incubator (Thermo Scientific) at 37 °C for the duration of the experiment.

At Day 4, after 96 h elapsed, final absorbance measurements were made on the Epoch spectrophotometer at 999 nm, and samples were characterized using transmission electron microscopy (TEM), Raman spectroscopy, and visible-near infrared (vis-NIR) absorbance spectroscopy.

2.1.1.2 Characterization of o-SWCNTs and MPO

TEM Microscopy

Samples of SWCNT at 1 mg/mL were diluted 1:100 with nanopure water. 5 µL of the diluted sample was placed on a lacey carbon TEM grid (Pacific-Grid Tech). The grids were covered and dried in ambient conditions over night before imaging (FEI Morgagni, 80 keV)

Raman Microscopy

100 uL samples were deposited on a quartz microscope slide and dried. Spectra were collected on a Renishaw inVia Raman microscope with an excitation wavelength of 633 nm. Spectra were acquired

over 100 to 3100 cm^{-1}. Exposure time was 15 seconds with 5 averaged scans per sampled location. 5 scans were conducted per sample.

Vis-NIR absorbance Spectroscopy

Untreated 150 µL samples analyzed with a Lambda 900 spectrophotometer (Perkin Elmer) using 200 µL quartz cuvettes (path length: 1 cm, World Precision Instruments, Inc.). Spectra were acquired over 500 to 1250 nm.

Electron paramagnetic resonance spectroscopy

The production of ascorbate radicals was observed using a JEOL-RE1X EPR spectrometer (Tokyo, Japan) in 50 mM phosphate buffer, containing 100 µM DTPA at 25 °C. The measurements were performed on 100 µL samples containing 15 µg SWCNT, 30 nM MPO, 100 µM H_2O_2, 140 mM NaCl and 1.0 mM AA. The sample was placed in gas-permeable Teflon tubing (0.8mm internal diameter, .013 mm thickness) from Alpha Wire Corp. (Elizabeth, NJ). The tubing was folded twice and placed in a 3.0 mm EPR quartz tube. The instrument values were: 355.0 G center field, 50 G sweep width, .79 G field modulation, 20 mW microwave power, 0.1s time constant, 1000 receiver gain, 2min time scan. The spectra were collected with EPRwase software (Scientific Software Services, Bloomington, IL).

Monitoring MPO activity with Amplex Red

MPO activity of the as-received and buffer-exchanged MPO was measured using Amplex Red for the (-) Cl^- samples with and without antioxidants. The stock Amplex Red solution (10mM in DMSO) was added in 3 µL aliquots to samples according to Table A2. Fluorescence-based kinetic spectra were acquired with a Fluoromax 3 (Horiba Scientific, Edison, NJ, USA) by acquiring measurements in 5 s intervals for 120 s at an excitation wavelength of 575 nm and 585 nm emission wavelength.

2.1.2 Results and Discussion

2.1.2.1 Characterization of o-SWCNTs

O-SWCNTs were characterized before and after degradation with MPO by TEM (Figure 10) and by Raman and UV-vis spectroscopy (Figure 11). TEM indicated that the o-SWCNTs were approximately 1 μm in length before degradation. In the presence of MPO, H_2O_2, and chloride ion, only amorphous carbonaceous material is observable which indicates a high degree of degradation. Micrographs taken from MPO active samples in the absence of chloride reveal a mixture of shortened nanotubes and carbonaceous amorphous debris. The addition of AA and GSH to the chloride containing experiment significantly mitigated the degradation of o-SWCNTs which is evidenced by the TEM micrographs of cylindrical o-SWCNTs in large aggregates. Similar aggregation and morphology is observed in the active MPO experiment without chloride and with antioxidants.

Raman spectroscopy data supports the TEM observations and provides some insight into the mechanism of degradation by MPO. The o-SWCNTs before degradation displayed peaks for the radial breathing mode (RBM, 147 cm^{-1} and 159 cm^{-1}, D (1348 cm^{-1}), G (1592 cm^{-1}) and 2D (2643 cm^{-1}) with a D/G ratio of .53. The (+) chloride system resulted in a spectrum devoid of characteristic Raman peaks, indicating complete degradation. The system containing MPO and H_2O_2 showed persistent o-SWCNT Raman bands throughout the experiment, however the RBM and 2D bans were comparatively suppressed and an increase in D/G ratio from .53 to .65 was observed. The relative increase in D band intensity was due to an increase in defects within the graphitic lattice incurred by reactive intermediates. For all antioxidant containing samples, the o-SWCNT Raman peaks remained essentially unchanged, thus indicating their effectiveness in mitigating biodegradation.

Further insight on the degradation process may be gained by an analysis of the shift in RBM during degradation. Raman signals were obtained primarily from metallic nanotubes due to resonant Raman

scattering of the 633 nm laser which is close in energy to the M_{11} electronic transition.[54] The o-SWCNTs displayed RBM peaks centered at 147 cm^{-1} and 159 cm^{-1}, which, according to Equation 5 correspond to nanotubes of approximately 1.52nm and 1.42 nm in diameter, respectively. While the RBM was not observed in the (+) Cl^- experiment, a shift in RBM to 170 cm^{-1} was observed for the active (-) Cl^- conditions. This shift is evidence for the degradation of larger diameter nanotubes and alludes to the possibility that MPO may favor larger diameter o-SWCNTs for degradation in the absence of Cl^-.

The o-SWCNT sample exhibited a broad UV-vis absorption spectrum (Figure 11) with distinct peaks, namely the S_{22} and M_{11} bands, respectively indicating the presence of semiconducting and metallic nanotubes. The near total disappearance of S_{22} and M_{11} bands in the (+) Cl^- degradation trial was observed along with a large decrease in overall absorbance. The reduction of both bands serves as evidence that chloride conditions degrade nanotubes without specificity. A similar reduction was observed for both bands in the chloride-free enzymatic conditions. Integration of the S_{22} peak relative to the baseline (Table A3) revealed that the chloride-free conditions exhibited a 2.7x decrease in comparison to a 4.1x reduction in the chloride conditions. The peak reduction for chloride-free conditions suggests that reactive intermediates are capable of degrading o-SWCNTs, but are outpaced by hypochlorous acid. Trials with and without chloride and either antioxidant exhibited a persisting S_{22} band, providing further evidence to the mitigating effect of antioxidants.

In addition to the broad spectrum UV-vis analysis, absorption measurements at 999 nm were made for all samples using a microplate reader. The S_{22} band was chosen as scattering less than 8%in the range of 800 nm to 1300 nm, thus ensuring the measured signal is largely due absorption.[55] The results (Figure 11) support the previous measurements, showing enhanced degradation in the chloride conditions with a 75% peak reduction after 4 days and a 60% reduction in the chloride-free samples. A small degree of degradation is observed in samples containing antioxidants with and without chloride, again indicating that antioxidants hinder both reactive intermediate and hypochlorite mediated biodegradation. In

addition, the effect of antioxidants concentrations was studied with this method (Figure A2). The aforementioned trials were repeated with additions resulting in final concentrations of 200 µM AA and 50 µM GSH (Table A4). Even at significantly lower concentration both antioxidants retained the same degree of effectiveness.

2.1.2.2 Mechanism of o-SWCNT Degradation by MPO

Characterization by UV-vis, TEM and Raman spectroscopy verify that o-SWCNTs are degraded with chloride, however the extent of degradation appears to depend on the reduction potential of the oxidants. In terms of reduction potential, HOCl with a potential of 1.48 V[56], and MPO's reactive intermediates, with a potential of 1.16 V, are both capable of oxidizing SWCNTs since its reduction potential is significantly lower at 0.5V.[56] However, the results clearly indicate that the reactive intermediates are less efficient than HOCl. It is likely that this discrepancy arises from the slow kinetics of o-SWCNT binding to an ideal docking site on MPO for degradation. Molecular simulations[44] have shown that o-SWCNTs must dock closely to MPO's active site in order to undergo degradation through reactive intermediates. In an aqueous solution of pH 7.4, the carboxyl groups of o-SWCNTs are highly anionic due to their pK_a of 5.5,[57] which allows electrostatic interaction with the highly cationic [43] MPO. The simulation reveals that the carboxyl groups at the o-SWCNT terminus must interact in a specific configuration with the positively charged arginine residues to allow close proximity to the heme group. Once the o-SWCNTs have reached the proper configuration, they may interact with the catalytically active tyrosine residues, Tyr 292 and Tyr 313.[58] In comparison to the fast reaction kinetics of freely diffusing HOCl, the slower kinetics of o-SWCNT docking and degradation by reactive intermediates are likely the source of the observed inefficiency of biodegradation in chloride-free conditions.

A direct reaction between antioxidant and o-SWCNT may also be a factor in biodegradation. As a result of the harsh oxidation process a multitude of defects incurred in the o-SWCNT in the form of lattice vacancies or hydroxyl, carbonyl, epoxide, and carboxyl functional groups.[59] Since it has been demonstrated that AA[60] and GSH[61] can reduce these oxygen-containing functional groups in the analogous graphene oxide system, it is reasonable to assume that this same process will occur with o-SWCNTs. This reaction would result in a more pristine nanotube structure, and would be evident in a reduction of the D/G ration in the Raman spectra. Indeed, this phenomena is observed for o-SWCNTs incubated with AA and GSH in non-active enzymatic conditions. Under these conditions, the D/G ratio decreases from .53 to .30 and from .31 to .30 for AA and GSH, respectively. Previous reports show that nanotubes with pristine structure are resistant to degradation. This raises the possibility that antioxidants mitigate degradation not only through a competitive reaction between reactive species, but also by reducing the o-SWCNTs susceptibility to attack. To address this possibility, o-SWCNTs were incubated with AA and GSH for four days at 37 °C prior to subjection to the original degradation conditions for another four days. After degradation, absorbance measurements at 999 nm using the microplate reader displayed significant decreases of 70% and 65% for AA and 64% and 69% for GSH in chloride and chloride-free conditions, respectively. Since the extent of degradation observed in these trials is comparable to the results without antioxidant pre-treatment, it can be concluded that neither antioxidant is capable of reducing the carboxyl groups, which are a critical component MPO catalyzed o-SWCNT degradation.[56]

Given that AA and GSH do not prevent o-SWCNT degradation by reduction, it is likely that competitive reactions between the antioxidants and peroxidase system components are responsible for the observed mitigation. In the chloride containing system, HOCl will be readily reduced by AA and GSH, thus preventing a reaction with the o-SWCNTs as shown in Figure 12. In the absence of chloride, AA and GSH will likely interfere with o-SWCNT degradation through distinct and different mechanisms. AA, with a low standard reduction potential[62] of .066 V is likely to reduce Compounds I and II of the peroxidase

cycle which has a mean reduction potential of 1.16V (Figure 12).[56] Since electron paramagnetic resonance spectroscopy (Figure A3) demonstrates the presence of the ascorbate radical and it has been shown that H_2O_2 cannot independently oxidize AA,[63] then AA is likely serving to outcompete o-SWCNTs as a substrate for MPO. GSH, a poor substrate for MPO,[64] demonstrates equal effectiveness to AA in preventing o-SWCNT degradation in all trials. However, H_2O_2 is capable of directly oxidizing GSH,[65] which would effectively prevent the activation of the peroxidase system

2.1.3 Conclusion

Through microscopic and spectroscopic examination of the peroxidase system, it can be concluded that both reactive intermediates and hypochlorite are responsible for the biodegradation of o-SWCNTs. It is also evident that the endogenous antioxidants, L-ascorbic acid and L-glutathione, are capable of significantly mitigating the MPO-catalyzed biodegradation, an effect which can be understood in terms of reduction potentials. Furthermore, while the antioxidants have been shown to reduce o-SWCNTs to a more pristine state, this phenomena does not significantly affect the biodegradation process.

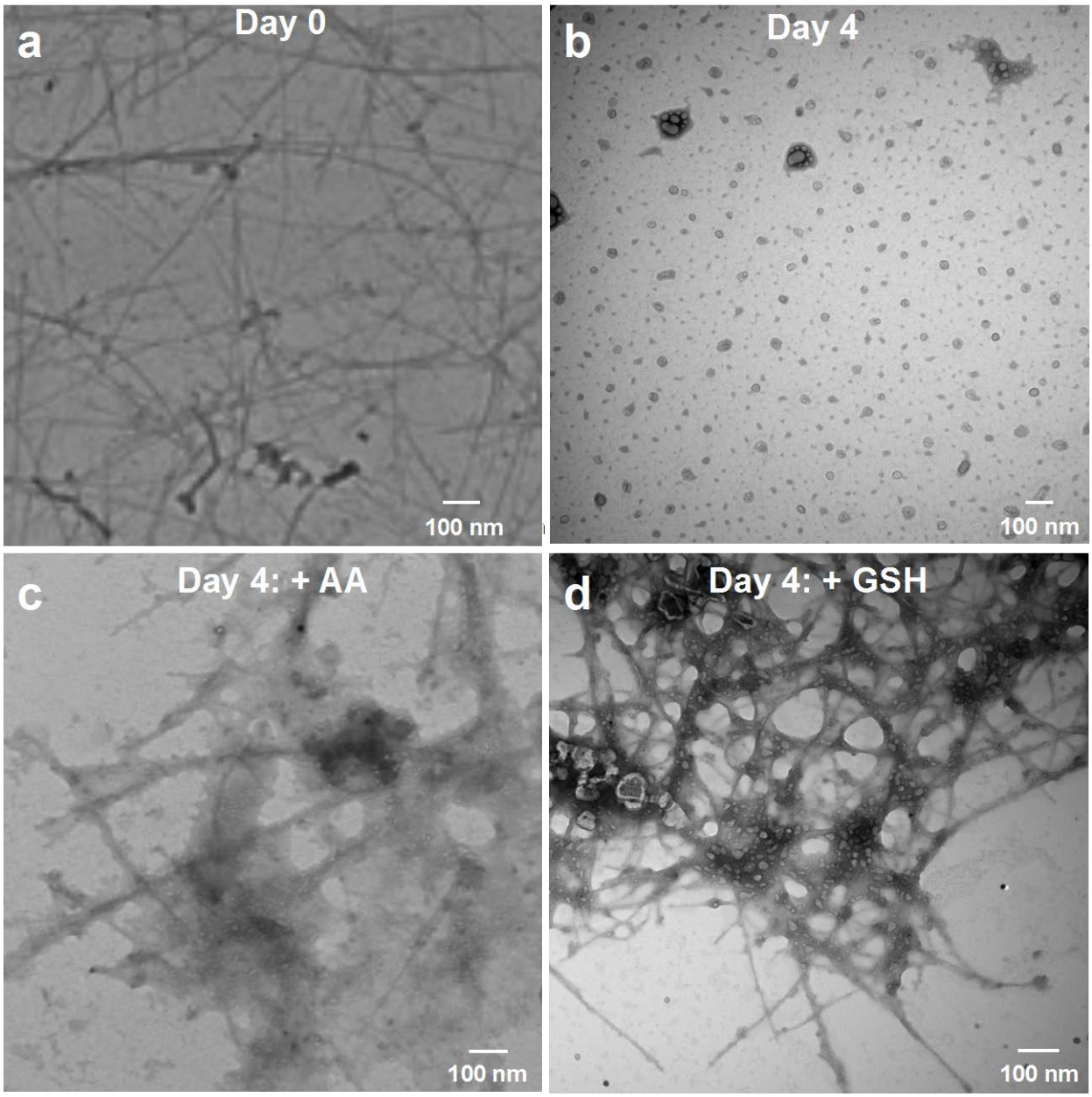

Figure 10: TEM images of o-SWCNTS in .1M phosphate buffer with 125 nM MPO and 140 mM NaCl. Micrographs were taken at a) day 0 and b) day 4 for the o-SWCNT + MPO + H_2O_2 + NaCl system. Images were taken under identical conditions for the c) ascorbic acid and d) glutathione systems at day four. Adapted from reference 45.

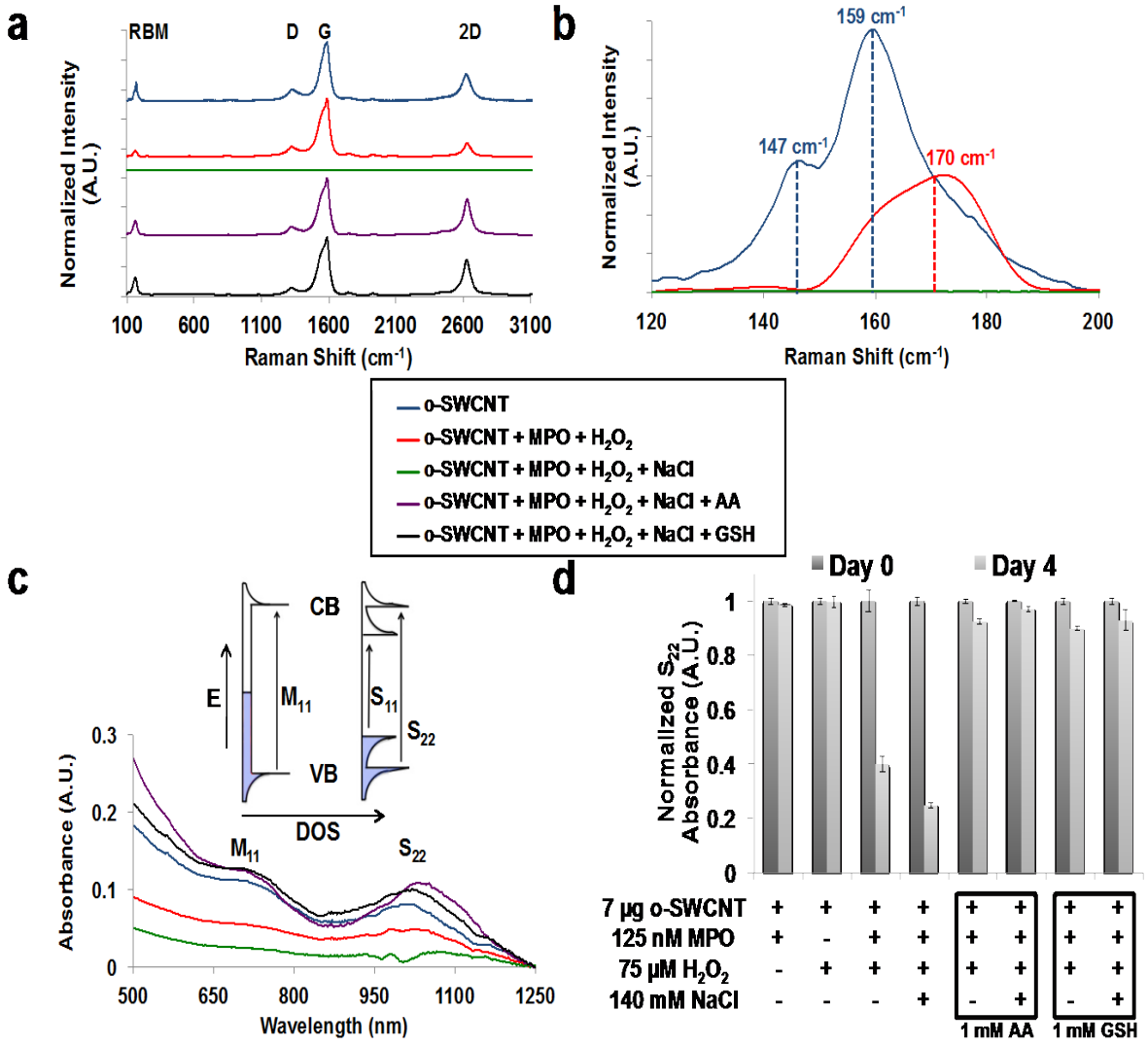

Figure 11: a) Raman spectroscopy on selected o-SWCNT samples on day 4. The RBM, D, G, and 2D bands are labeled. b) Zoom-in of radial breathing mode for selected o-SWCNT samples on day 4. c) vis-NIR absorption spectra of selected samples from (a). Inset depicts the DOS and relevant electronic transitions for metallic (left) and semiconducting (right) o-SWCNTs. d) Bar graph depicted the change in absorbance near the S_{22} transition for the experimental conditions indicated by (+/-). Data was obtained by microplate reader, and the error bars show standard error of the mean for a sample size of three. Adapted from reference 45.

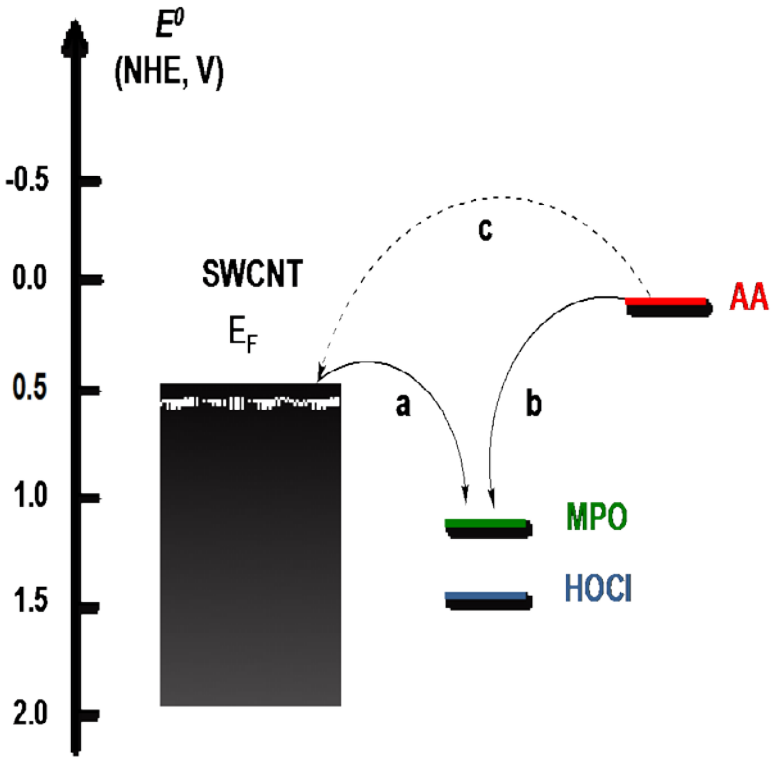

Figure 12: Schematic depicting the standard reduction potentials of SWCNTs (E^0 = .5V), MPO reactive intermediates (E^0 = 1.16V), HOCl (E^0 = 1.48V), and AA (E^0 = .066V). MPO and HOCl will oxidize (a) SWCNTs and (b) AA due to their favorable reduction potentials. AA is also capable of (c) reducing SWCNTs in this scheme. Adapted from reference 45.

2.2 Enzymatic Oxidation of PEG-Functionalized Carbon Nanotubes

This section explores the susceptibility of polyethylene glycol-coated SWCNTs and o-SWCNTs to *in vitro* biodegradation by MPO under conditions similar to the previous section. The material contained here was published as a research paper[66] in the journal *Nanoscale.*

List of Authors: Kunal Bhattacharya, Cristiano Sacchetti, Ramy El-Sayed, Andrea Fornara, Gregg P. Kotchey, James A. Gaugler, Alexander Star, Massimo Bottini, and Bengt Fadeel.

Author Contributions: CS and MB fabricated SWCNTs and performed physicochemical analysis with AFM and DLS. GPK, JAG, and AS designed *in vitro* MPO degradation experiments. GPK and JAG performed *in vitro* MPO degradation experiments. JAG performed absorption and Raman spectroscopy.

2.2.1 Experimental Details

2.2.1.1 Functionalization and Characterization of SWCNT

Fabrication of PEG-Coated SWCNTs (cPEG-SWCNTs)

Pristine SWCNTs (Carbons Solutions, Inc.) were oven dried and mixed in a 1:5 weight ratio with 1,2-distearoyl-*sn*-glycero-3-phophoethanolamine-N-[amino(polyethylene-glycol)-2000] (Avanti Polar Lipids, Inc.) in PBS. After 6h sonication, the coated CNTs were fractionated were fractionated by stepwise centrifugation to collect short hydrophilic amino-terminated coated CNTs. The collected CNTs were dialyzed in a 100 kDa-cut off membrane to remove free phospholipids.

Fabrication of Covalently Functionalized PEG- SWCNTs (fPEG-SWCNTs)

Three milligrams of oven-dried ox-SWCNTs (Carbon Solutions, Inc.) were added to α-amino-ω-Boc-amino linear 2, 5, or 10 kDa PEG (Rapp Polymere GmbH) in 10 mL of dichloromethane, 125 µL of 1 M

N,*N*'-dicyclohexylcarbodiimide and 60 mg of 4-dimethylaminopyridine (Sigma-Aldrich). The amidation reaction continued for 48 h and Boc groups were unprotected with trifluoroacetic acid solution in a 1:1 (v/v) ratio in dichloromethane. Short amino-terminated fPEG-SWCNTs were collected with fractionation by stepwise centrifugation and dialyzed with a 100 kDa-cut off membrane.

Atomic Force Microscopy (AFM)

Several microliters of each nanotube solution was pipetted onto a separate mica substrate (Ted Pella). The substrate was then rinsed in Milli-Q H_2O and dried under a nitrogen stream. The nanotubes were imaged using a 5500 AFM (Agilent Technologies, Inc.). Twenty longitudinal line scans were acquired for each type of nanotube.

Raman Spectroscopy of SWCNTs

Spectra of all SWCNTs were acquired on day 0 and day 7 of the degradation experiment using a Horiba XploRA ONE Raman microscope. The spectra were acquired using a 638 nm laser and an Olympus MPLN objective with an NA of .90. The signal was acquired for 1 s under 100x magnification. Three spectra were acquired for each sample with 20 repeated acquisitions averaged for a single spectra. The D-band (~1350 cm^{-1}) and G-band (~1598 cm^{-1}) peak areas were integrated to create a D/G ratio for each measurement and averaged with standard error (S.E.).

NIR Spectroscopy of SWCNTs

An Epoch microplate spectrophotometer (BioTek, Winooski, VT) was used to record absorbance values at 999 nm each day from day 0 to day 7. The absorbance spectra at 999 nm were measured daily using the Epoch microplate reader and the relative change in absorbance was plotted with standard deviation error bars representing a sample size (n) of six. One-way ANOVA was performed to compare relative change between day 0 and day 7.

2.2.1.2 Enzymatic Degradation of PEG-SWCNT

Lyophilized purified native human myeloperoxidase (Athens Research and Technology, Inc.) was dissolved in 133 µL of nanopure water to create a ~5 µM stock solution. Stock solutions of 50 mM H_2O_2 and 5M NaCl were made in nanopure water as well. Solutions of 250 µL of 0.1M phosphate buffer containing 50 µM DTPA, 140 mM NaCl, 100 nM MPO and 15 µg of each nanotube sample were created in sets of six. Every hour additions of 50 mM H_2O_2 were made to create a 200 µM final concentration in the sample. Additions were repeated seven times a day for a seven day duration. Also, daily additions of MPO were made for a final concentration of 100 nM MPO. Samples were analyzed daily using NIR-spectroscopy. Raman spectroscopy was used to analyze the samples at day 0 and day 7.

2.2.2 Results and Discussion

2.2.2.1 Characterization of SWCNTs

Based upon AFM measurements (Figure 13), the lengths of the SWCNTS were relatively similar across all samples. The average height (Table 1) of cPEG-SWCNTS was ~1 nm and the average height of fPEG-SWCNTS was 7 nm. The height values for cPEG-SWCNTs indicate that the PEG chains were mostly laying on their side, while the PEG chains on the fPEG-SWCNTs were protruding vertically from the nanotube sidewall. A Kaiser test was previously conducted[67] to assess PEG surface coverage of the SWCNTs (Table 1) by measuring the number of free amine groups on the amine-terminated PEG chains. The coverage of cPEG-SWCNTs was markedly lower than that of fPEG-SWCNTs at ~0.1 mmol $g^{-1}$and .4 mmol g^{-1} SWCNT. Consideration of the AFM height values and surface coverages suggests that cPEG-SWCNTs are not fully coated, where fPEG-SWCNTs are densely functionalized.

2.2.2.2 Enzymatic Degradation of PEG-SWCNTs

After seven days of SWCNT *in vitro* MPO biodegradation nanotubes were analyzed using NIR (Figure 15) and Raman spectroscopy (Figures 15, A2) to determine the effect of PEG functionalization and the extent of SWCNT degradation. Significant increases in the D/G ratio were observed for the 2-kDa, 5-kDa, and 10-kDa fPEG-SWCNT, along with a miniscule increase for the 2-kDa cPEG-SWCNT. Interestingly, a slight decrease in D/G ratio was observed for the unfunctionalized pristine and o-SWCNT. The Raman spectra of the fPEG-SWCNT (Figure 14) show a trend of decreasing final D/G ratio with increasing PEG chain length, which indicates that the mitigation of biodegradation is dependent on higher PEG-chain lengths. While this trend is supported in the NIR-data (Figure 15) for both 2-kDa and 5-kDa PEG chains, the 10 kDa measurements displayed a large margin of error which prevented a confident comparison. In accordance with previously established literature[68], the pristine, carboxyl-free cPEG-SWCNT did not undergo significant degradation. This conclusion is supported by the miniscule shifts observed in the D/G ratio (Figure 14) and NIR data for cPEG-SWCNT. In previous studies,[69–71] o-SWCNTs were shown to efficiently degrade within 24 h, thus o-SWCNTs were chosen as a positive control. As expected, a large decrease in S_{22} band absorbance was observed in the NIR spectra (Figure 15), which indicates the degradation of o-SWCNTs. However, a counter-intuitive decrease in the Raman D/G ratio was reported for day 7. This measurement is likely an artifact of biased spectra acquisition. At day 0, an abundance of o-SWCNTs were observed in the Raman sample, and at day 7 it became extremely difficult to detect an o-SWCNT spectra. After much effort, it was possible to acquire an o-SWCNT spectra, however, a blank spectra would have been representative of the sample's o-SWCNT scarcity.

The extent of degradation observed for the PEG-SWCNTs is relatively lower in comparison to a previous study by Vlasova *et al*.[72] The comparative reduction in biodegradation efficacy is likely due differences in in experimental design and SWCNT functionalization. The latter study utilized PEG-SWCNTs with significantly lower PEG grafting density (10-25%) and low MW PEG chains (600 Da), along with a

100% higher concentration of MPO. Since the protein corona-type interaction[44] requires physical contact, this important degradation pathway may be prevented by a high degree of PEGylation.

2.2.3 Conclusion

AFM measurements, in tandem with the Kaiser test, confirmed the high degree of covalent functionalization for fPEG-SWCNTs and a lower degree of non-covalent functionalization for the cPEG-SWCNTs. Previous literature reports were validated by the observations that the carboxyl-free cPEG-SWCNT did not undergo significant degradation. Significantly, the high degree of PEGylation observed for the fPEG-SWCNTs was shown to retard MPO degradation, with the effect enhanced by increasing chain length.

a)

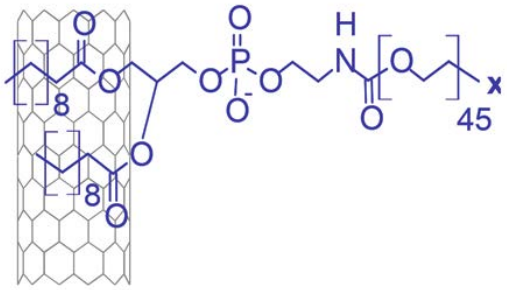

2 kDa cPEG-SWCNT-m: x = CH_3

b)

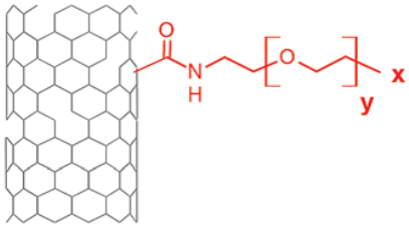

2 kDa fPEG-SWCNT-m: x = CH_3, y = 45
5 kDa fPEG-SWCNT-m: x = CH_3, y = 113
10 kDa fPEG-SWCNT-m: x = CH_3, y = 225

c)

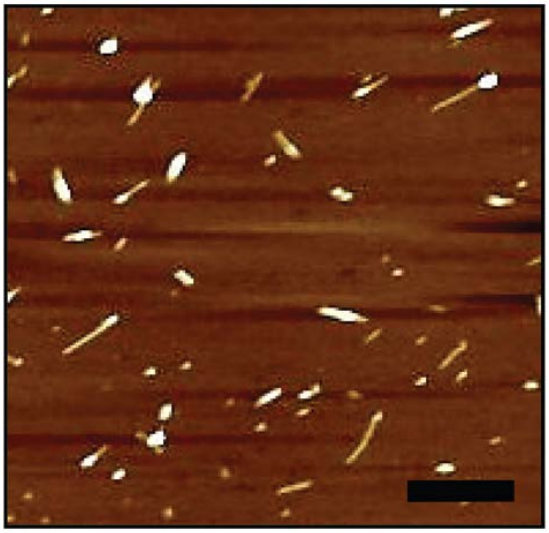

Figure 13: a) Non-covalently functionalized PEG-coated SWCNT (2-kDa cPEG-SWCNT) by adsorption of phospholipid modified amino-terminated PEG. b) Covalently functionalized o-SWCNT with linear 2-kDa, 5-kDa, and 10-kDa amino-PEG-boc chains. c) AFM image of 2-kDa cPEG-SWCNT in a 2.5 x 2.5 µm region. Scale bar is 300 nm. Adapted from reference 77.

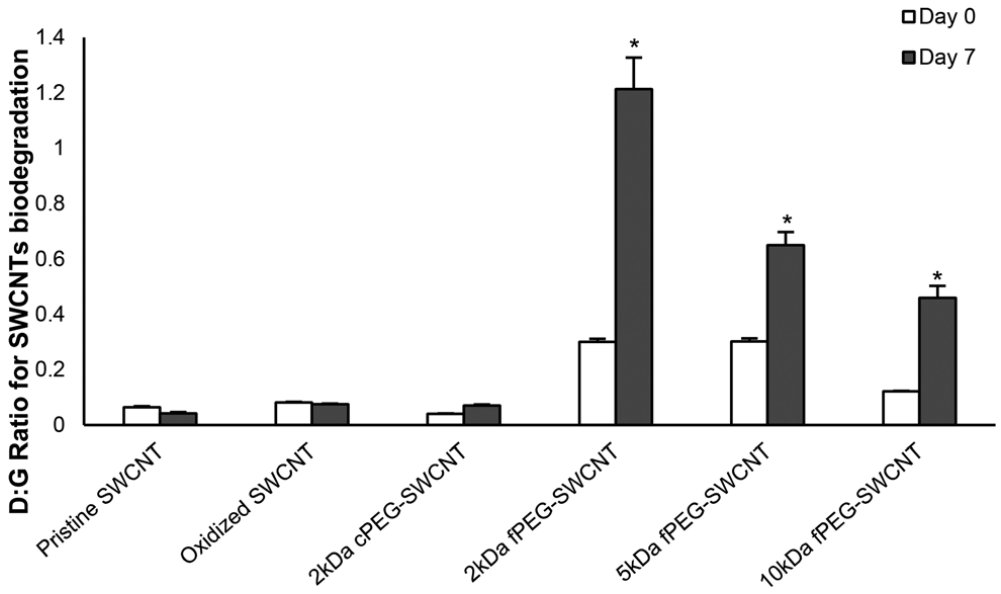

Figure 14: D/G ratio for o-SWCNT samples in the presence of MPO + H_2O_2 + Cl^- at day 0 and day 7. P values * ≤ 0.05 by 2-tailed t-test for averaged measurements of three different spots per sample. Adapted from reference 77.

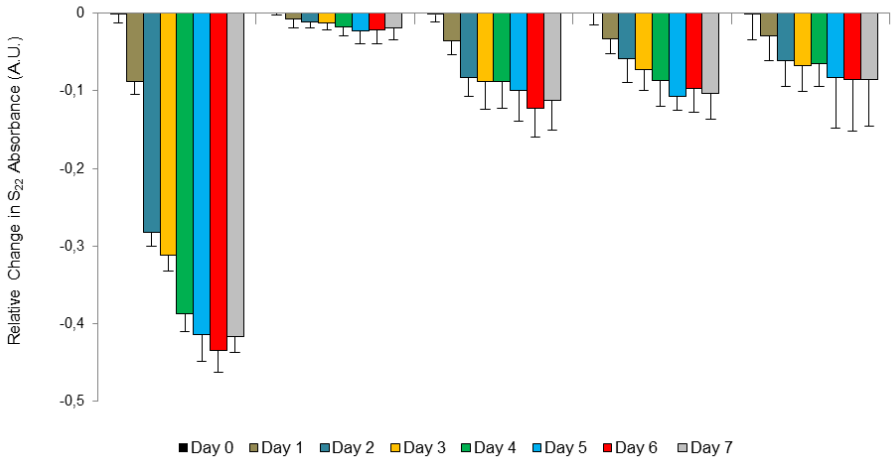

Figure 15: Relative absorbance changes near the SWCNT S_{22} transition for o-SWCNT samples in the presence of MPO + H_2O_2 + Cl^-. Error bars represent one way ANOVA, followed by Turkey post-hoc test for a sample size of six. *p* values * ≤ 0.05, ** ≤ 0.01, *** ≤ 0.001. Adapted from reference 77.

Table 1: Physico-chemical characterization. Length and PEG average height were measured using AFM

	o-SWCNT	2-kDa cPEG-SWCNT	2-kDa fPEG-SWCNT	5-kDa fPEG-SWCNT	10-kDa fPEG-SWCNT
Surface Functional Group	-COOH	$-CH_3$	$-CH_3$	$-CH_3$	$-CH_3$
Length (nm)	245 ± 105	142 ± 49	129 ± 48	130 ± 39	146 ± 51
PEG density (mmol g^{-1})	n/a	0.12 ± 0.04	-	0.39 ± 0.1	-
PEG height (nm)	n/a	1.2 ± 0.6	7.2 ± 3	9.3 ± 2.9	10.4 ± 2.8

Adapted from reference 77.

3.0 Separation of Nitrogen-Doped Carbon Nanocups

Nitrogen-doped multi-walled carbon nanotubes, (N-MWCNTs) with high nitrogen content possess a distinct and well-defined stacked-cup morphology. These nitrogen-doped nanocups (NCNCs) were hypothesized to possess a near-ideal structure for mechanical separation and individualization, as the NCNCs do not nest within one another (Figure 16a), a common trait of low-nitrogen % N-MWCNT samples (Figure 16b). Mechanical separation was effected by milling with a mortar and pestle which yielded well-separated NCNCs of relatively high structural integrity (Figure 17c). The NCNCs were suspended in an aqueous sodium dodecyl sulfate solution and enriched by centrifugal sedimentation of impurities. Additionally, these NCNCs were observed to form a stable suspension (Figure 17d) for over one week. The material contained in this section is original research in preparation for submission and publication.

List of Authors: James A. Gaugler, Sean Hwang, James A. Ellis, Alexander Star

Author Contributions: JAG and AS designed the experiments. JAG performed NCNC milling, dynamic light scattering, zeta potential measurement, transmission electron microscopy, and Raman microscopy. SH performed base-piranha/HCl treatment on as-received N-MWCNTs. JAE performed x-ray photoelectron spectroscopy.

3.1 Experimental Details

3.1.1 Purification and Separation of N-MWCNTs

Commercially acquired, ammonia-synthesized N-MWCNTs (Nano Tech Labs) were sequentially treated with base-piranha and concentrated HCl for 24 hours to remove amorphous carbon and residual metal catalyst.[78] After neutralization and drying, 6.01 milligrams of N-MWCNTs were milled in a mortar and pestle for 1 h, then collected and stirred for 24 hr in 12M hydrochloric acid to dissolve freshly exposed iron catalyst. The acid/N-MWCNT mixture was collected over a 200 nm hydrophilic PTFE membrane (Millipore) by vacuum filtration and washed over the filter with 100 mL of nanopure H_2O. The milled N-MWCNTs were then suspended at a concentration of 0.15 $\frac{mg}{mL}$ in an aqueous solution of 0.1 wt% SDS and sonicated for 30 minutes. The solution was split into equal portions of 4.8 mL and centrifuged for 1 h at 1,380 rcf using a Centrific Model 228 (Fisher Scientific). This resulted in the formation of a stable gray supernatant of colloidal NCNCs in which larger nanotube structures were eliminated to a significant extent. The yield of NCNCs in the supernatant was calculated to be 22%.

3.1.2 Characterization of N-MWCNTs and Separated NCNCs

X-ray Photoelectron Spectroscopy (XPS)

XPS spectra were acquired with an ESCALAB 250Xi XPS (Thermo Scientific) for base-piranha/HCl treated N-MWCNTs before and after milling by mortar and pestle. For both samples, high resolution spectra were obtained for carbon, oxygen and nitrogen.

Transmission Electron Microscopy

N-MWCNTs were imaged by TEM (FEI Morgagni, 80 keV). TEM images were taken before and after milling by mortar and pestle, and after centrifugation.

Zeta Potential Measurement

N-MWCNT were analyzed before and after milling, and after centrifugation on a PALS Zeta potential analyzer (Brookhaven Instruments Corp.)

Raman Microscopy

Raman spectra were acquired for N-MWCNT samples before and after milling by mortar and pestle using a Horiba XploRA ONE Raman microscope. The spectra were acquired using a 638 nm laser and an Olympus MPLN objective with an NA of 0.90. The signal was acquired for 1 s under 100x magnification. Three spectra were acquired for each sample with 20 repeated acquisitions averaged for a single spectra. The D-band (~1350 cm^{-1}) and G-band (~1598 cm^{-1}) peak areas were integrated to create a D/G ratio for each measurement and averaged over the sample size using standard error.

Dynamic Light Scattering

After centrifugation, DLS measurement was made on the supernatant containing NCNCs in a 0.1 wt% SDS suspension using a Malvern Zetasizer Nano ZS90.

3.2 Results and Discussion

N-MWCNTs determined to contain ~6% nitrogen by XPS were milled for one hour by mortar and pestle in ambient conditions. TEM observations showed that the NCNCs underwent a high degree of separation, however large, amorphous nanotubes were also present in the sample (Figure 17a). The Raman spectra before and after grinding (Figure C5) show an increase in the average D:G ratio from 1.56±0.2 to 1.93±0.18, indicating some damage was incurred to the sp^2 carbon lattice. However, TEM observations show that the NCNCs remain largely intact after milling. Interestingly, the XPS spectra (Figures C2 and C4) show that NCNCs increase in atomic oxygen % from 7% to 11% after grinding. This may be the result of a solid-state reaction between atmospheric oxygen or water and radicals formed by fracturing of the carbon lattice.[79] The increased oxygen content is supported by the observed increase in zeta-potential from -37 mV to -47 mV after grinding, which suggests an increased quantity of negatively charged oxygen functional groups. Centrifugation of NCNCs suspended in a 0.1% SDS solution significantly decreases NCNC polydispersity in the supernatant by inducing the sedimentation of larger, amorphous nanotube structures. TEM observations show an enrichment of shortened NCNCs in the supernatant and the migration of most amorphous nanotube structures to the pellet upon centrifugation. The observed reduction in polydispersity is further supported by DLS measurement (Figure C6) of the supernatant which shows a mean tumbling diameter of 238 nm with a range of 50 nm to 600nm. The aqueous NCNC solution (Figure 17d) remained stable over one week, thus providing evidence that NCNCs can form a stable colloid in dilute SDS solution. The colloidal stability of the separated NCNCs is supported by their highly negative zeta potential. The electrostatic repulsion between NCNCs due to their negative zeta potential, coupled with the surfactant effect of SDS[80], may explain their ability to form a stable colloid.

3.3 Conclusion

N-MWCNTs with a high nitrogen atomic % and pronounced stacked-cup morphology are efficiently separated into NCNCs of varying length by grinding with a mortar and pestle. The quantity of NCNC oxygen functional groups increases upon mechanical separation which may contribute to colloidal stability by electrostatic repulsion. The NCNCs form a stable colloidal suspension in aqueous 0.1 wt% SDS and the majority of amorphous structural impurities may be eliminated as sediment by centrifugation. The purification process results in a 22% yield. Lastly, the edges of the NCNC are relatively undamaged which may allow for the efficient corking of NCNCs, and their application as a drug delivery vessel.

a) **b)**

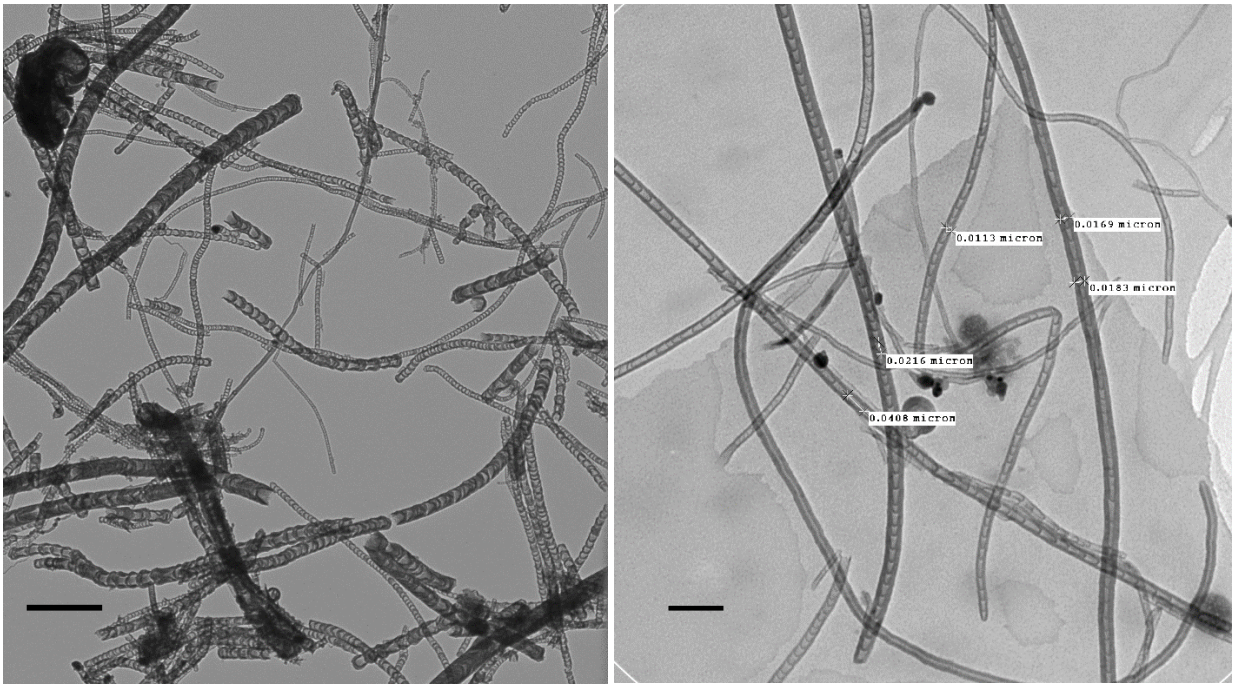

Figure 16: a) Nitrogen-doped multi-walled carbon nanotube displaying distinct stacked up structure. a) High nitrogen % N-MWCNTs with more disorder and less tightly associated NCNCs. b) Low nitrogen % N-MWCNTs showing tightly associated NCNCs. Scale bars are 500 nm and 100 nm, respectively

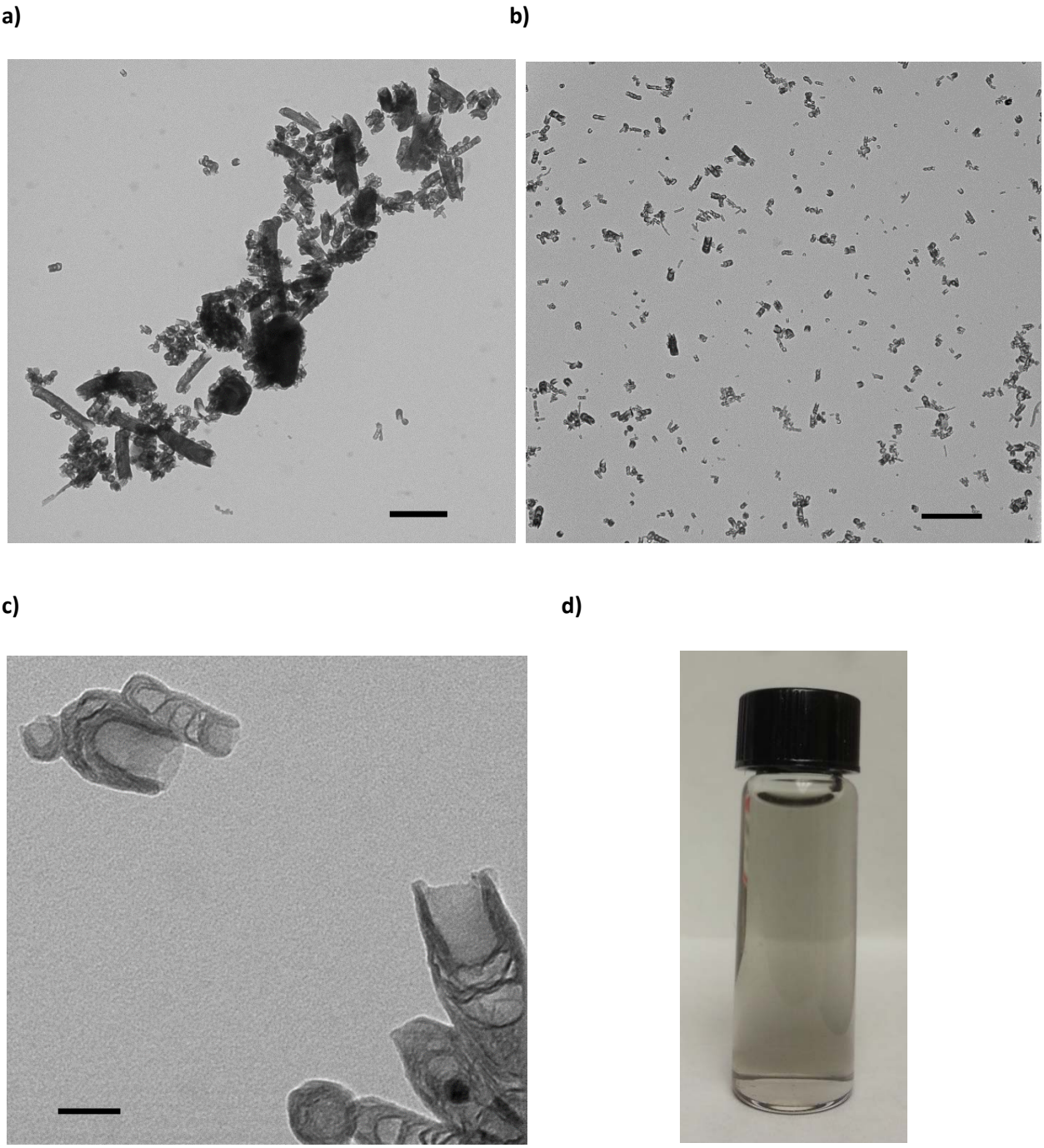

Figure 17: a) TEM micrograph of milled N-MWCNTs depicting high polydispersity in length. b) TEM micrograph of aqueous NCNC suspension after centrifugation. c) TEM micrograph depicting an intact NCNC edge. d) Optical image of aqueous NCNC suspension after one week. Scale bars are a) 600 nm, b) 800 nm, and c) 50 nm.

APPENDIX A

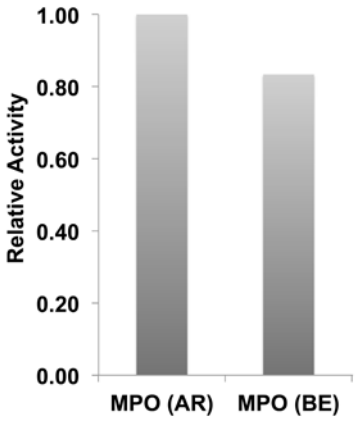

Figure A1: Relative active of buffer exchanged (BE) and as-received (AR) MPO calculated from the Amplex Red fluorescence-kinetic experiment.

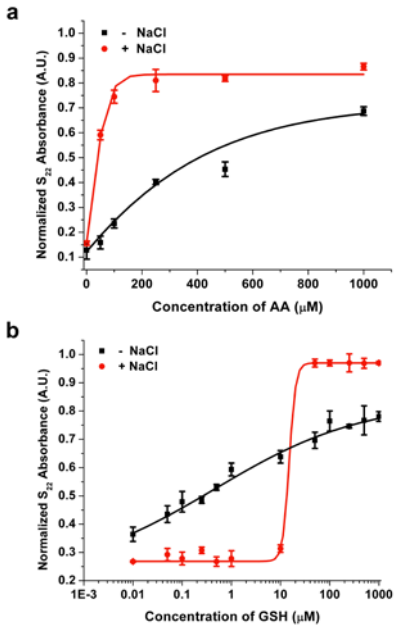

Figure A2: S_{22} absorbance measurements for varying concentrations of (a) AA and (b) GSH in conditons with chloride (red line) and without chloride (black line).

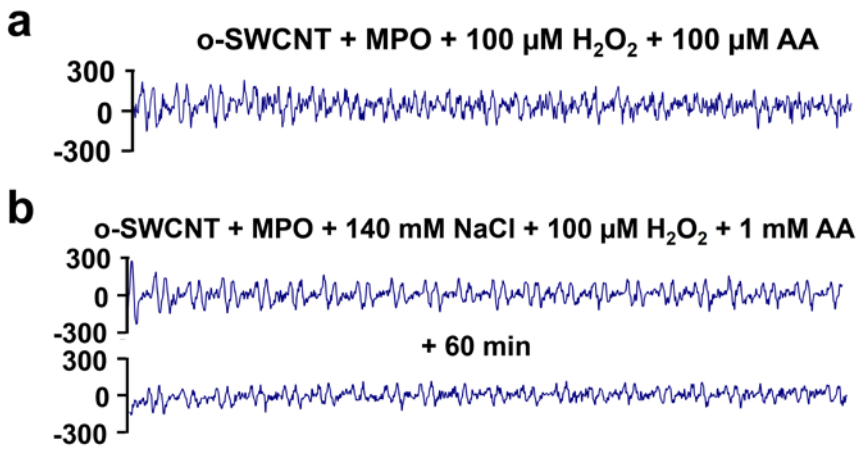

Figure A3: Electron paramagnetic resonance (EPR) study indicating the presence of the ascorbate radical (a) in chloride-free degradative conditions and (b) after 60 minutes of incubation in degradative conditions with chloride.

Table A1: Initial Experimental Conditions

Sample	o-SWCNTs (1 mg/mL)	H_2O_2 (18.75 mM)	AR MPO (2.0 µM)	BE MPO	NaCl (5 M)	AA (250 mM)	GSH (250 mM)	PB/DTPA (0.1 M/ 300 µM)
o-SWCNT	7 µL	0	0	0	0	0	0	243 µL
o-SWCNT + MPO	7 µL	0	0	4.8 µL	0	0	0	238.2 µL
o-SWCNT + H_2O_2	7 µL	1 µL	0	0	0	0	0	242 µL
o-SWCNT + MPO + H_2O_2 − Cl^-	7 µL	1 µL	0	4.8 µL	0	0	0	237.2 µL
o-SWCNT + MPO + H_2O_2 + Cl^-	7 µL	1 µL	4 µL	0	7 µL	0	0	231 µL
o-SWCNT + AA	7 µL	0	0	0	0	1 µL	0	242 µL
o-SWCNT + MPO + AA	7 µL	0	0	4.8 µL	0	1 µL	0	237.2 µL
o-SWCNT + MPO + H_2O_2 − Cl^- + AA	7 µL	1 µL	0	4.8 µL	0	1 µL	0	236.2 µL
o-SWCNT + MPO + H_2O_2 + Cl^- + AA	7 µL	1 µL	4 µL	0	7 µL	1 µL	0	230 µL
o-SWCNT + GSH	7 µL	0	0	0	0	0	1 µL	242 µL
o-SWCNT + MPO + GSH	7 µL	0	0	4.8 µL	0	0	1 µL	237.2 µL
o-SWCNT + MPO + H_2O_2 − Cl^- + GSH	7 µL	1 µL	0	4.8 µL	0	0	1 µL	236.2 µL
o-SWCNT + MPO + H_2O_2 + Cl^- + GSH	7 µL	1 µL	4 µL	0	7 µL	0	1 µL	230 µL

Table A2: Experimental Conditions for MPO Assay with Amplex Red

Sample	Amplex Red (10 mM)	H_2O_2 (10 mM)	AR MPO*	BE MPO*	AA (250 mM)	GSH (250 mM)	PB/DTPA (0.1 M/ 300 µM)
AR MPO + H_2O_2 − Cl^-	3 µL	3 µL	4 µL	0	0	0	590 µL
BE MPO + H_2O_2 − Cl^-	3 µL	3 µL	0	4.8 µL	0	0	589.2 µL
o-SWCNT + AR MPO + H_2O_2 − Cl^- + AA	3 µL	3 µL	4 µL	0	2.4 µL	0	587.6 µL
MPO + H_2O_2 − Cl^- + GSH	3 µL	3 µL	4 µL	0	0	2.4 µL	587.6 µL
*Diluted 1/200 with PB/DTPA							

Table A3: Area of S_{22} Absorbance Peak

Sample	Area of S_{22} Peak
o-SWCNT	8.135
o-SWCNT + MPO + H_2O_2	2.980
o-SWCNT + MPO + H_2O_2 + NaCl	1.962
o-SWCNT + MPO + H_2O_2 + GSH	7.425
o-SWCNT + MPO + H_2O_2 + NaCl + GSH	7.981
o-SWCNT + MPO + H_2O_2 + AA	9.698
o-SWCNT + MPO + H_2O_2 + NaCl + AA	10.627

Table A4: Initial Conditions for Experiments Varying Antioxidant Concentration

Sample	o-SWCNTs (1 mg/mL)	H_2O_2 (18.75 mM)	AR MPO (2.0 µM)	BE MPO	NaCl (5 M)	AA (250 mM)	GSH (250 mM)	PB/DTPA (0.1 M/ 300 µM)
o-SWCNT + MPO + H_2O_2 − Cl^- + AA	7 µL	1 µL	0	4.8 µL	0	1 µL	0	236.2 µL
o-SWCNT + MPO + H_2O_2 + Cl^- + AA	7 µL	1 µL	4 µL	0	7 µL	1 µL	0	230 µL
o-SWCNT + MPO + H_2O_2 − Cl^- + GSH	7 µL	1 µL	0	4.8 µL	0	0	1 µL	236.2 µL
o-SWCNT + MPO + H_2O_2 + Cl^- + GSH	7 µL	1 µL	4 µL	0	7 µL	0	1 µL	230 µL

All content of Appendix A was adapted from reference 45.

APPENDIX B

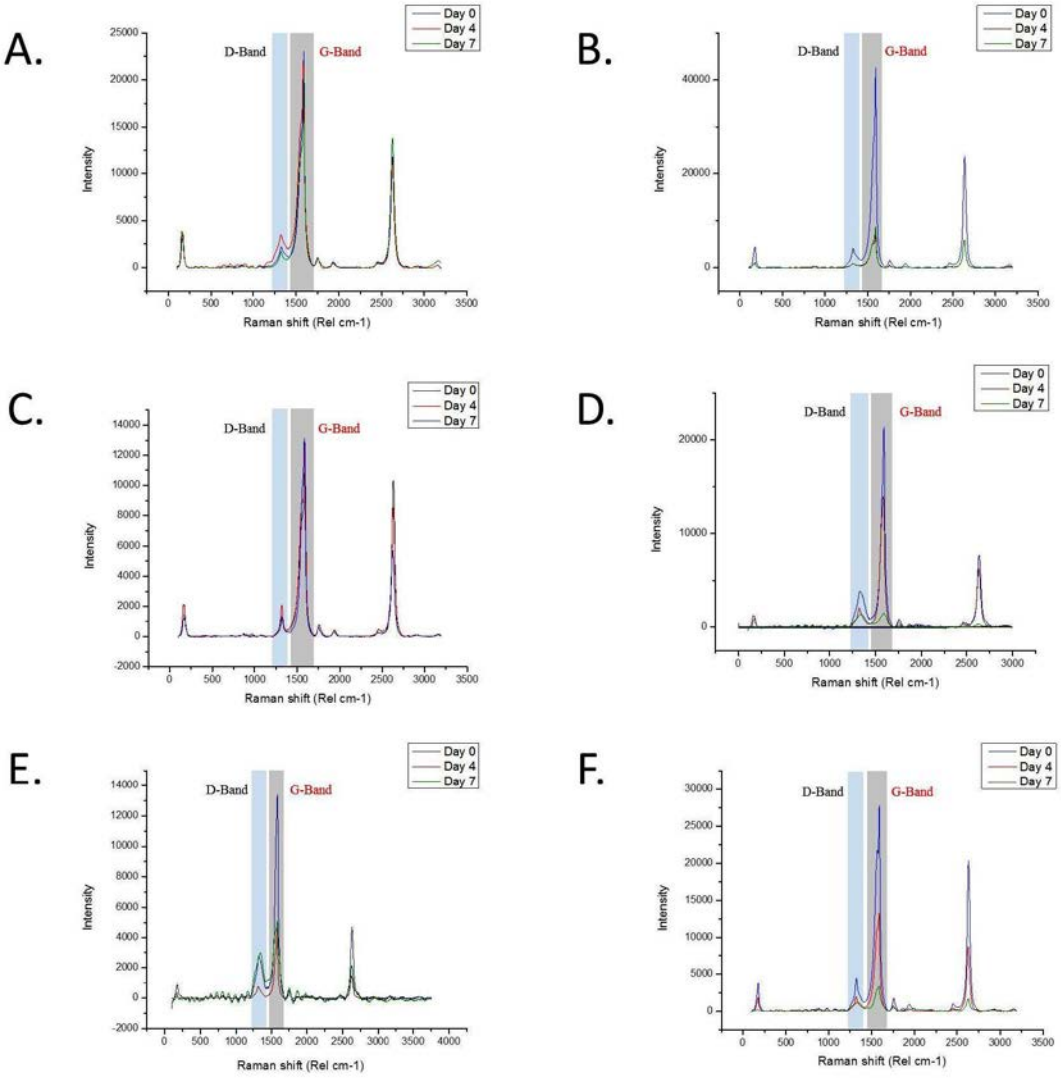

Figure B1: Raman spectroscopic analysis of MPO + H_2O_2 + NaCl degradation conditions of **a)** pristine SWCNTs, **b)** ox-SWCNTs, 2kDa cPEG-SWCNTs, **d)** 2kDa fPEG-SWCNTs, **e)** 5kDa fPEG-SWCNTs, **f)** 10kDa fPEG-SWCNTs. Measurements of biodegradation were performed on 0, 4 and 7 days by Raman spectroscopy. Adapted from reference 77.

APPENDIX C

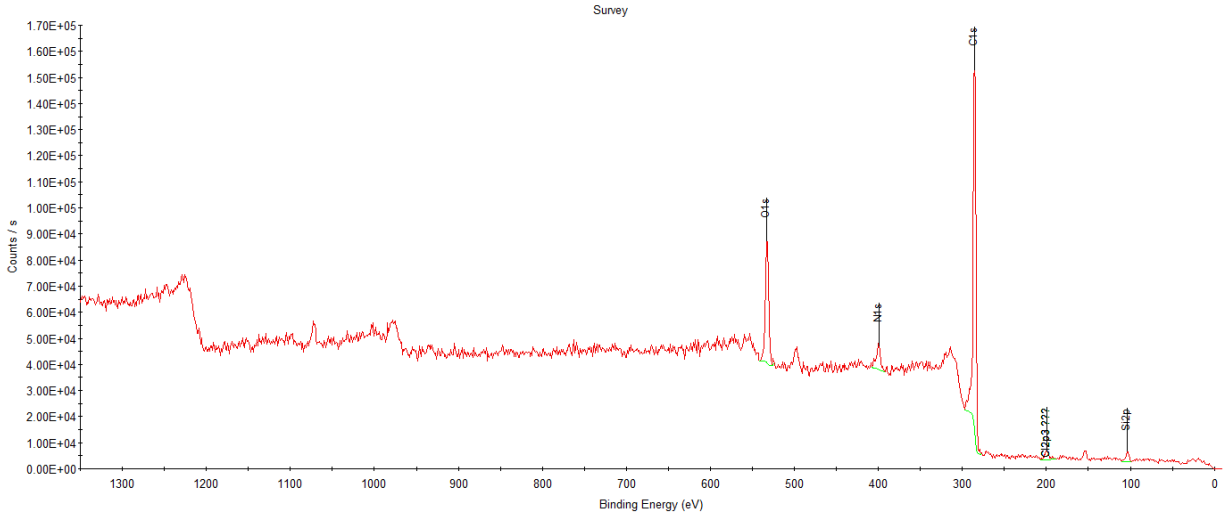

Figure C1: XPS Survey scan of piranha/HCl treated N-MWCNTs.

a)

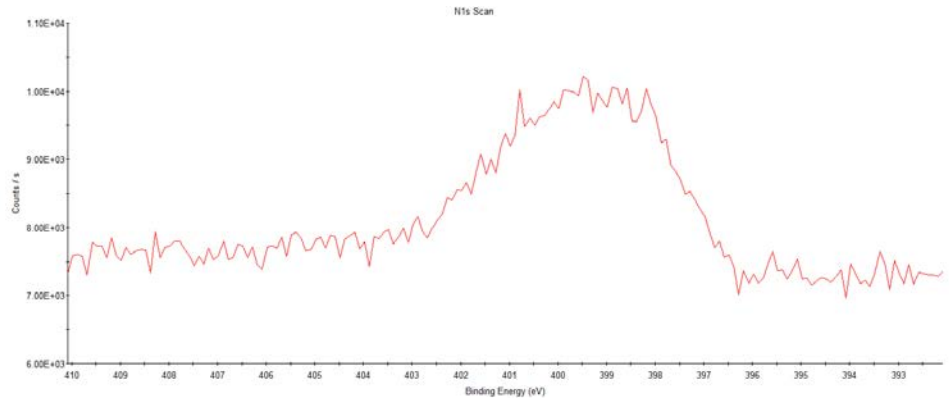

b)

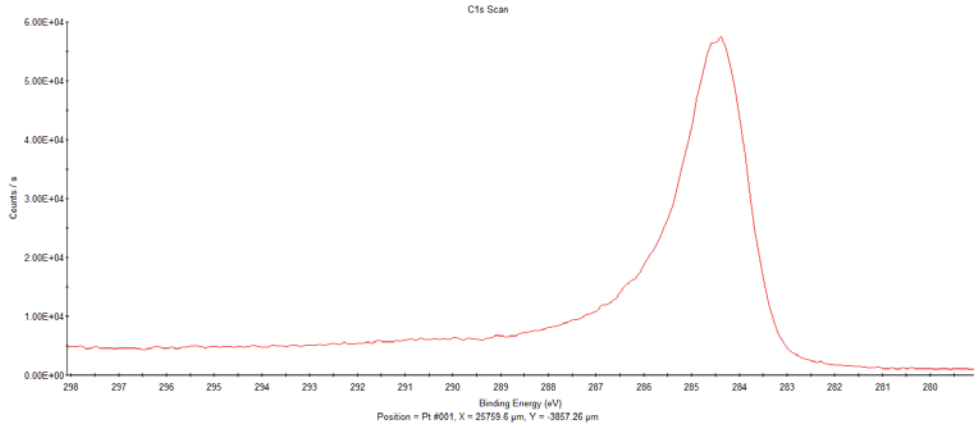

c)

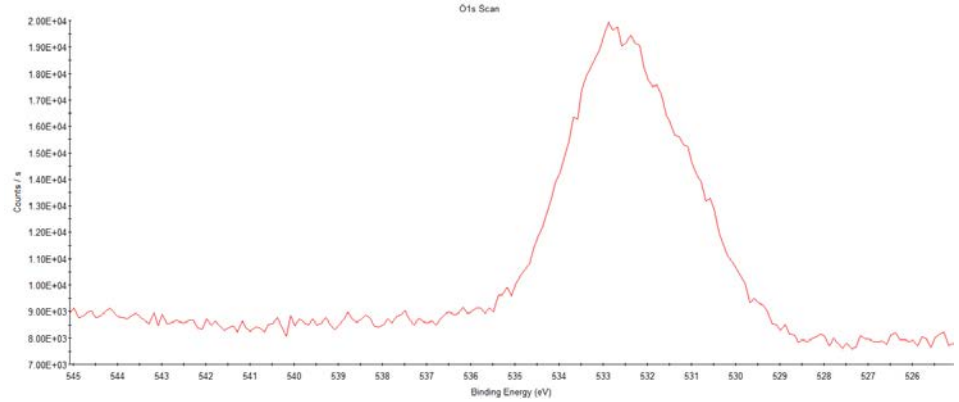

Figure C2: High resolution XPS spectra of commercial N-MWCNTs after base-piranha/HCl treatment, showing: a) nitrogen peaks, b) carbon peaks, and c) oxygen peaks. Atomic % values were obtained by integration

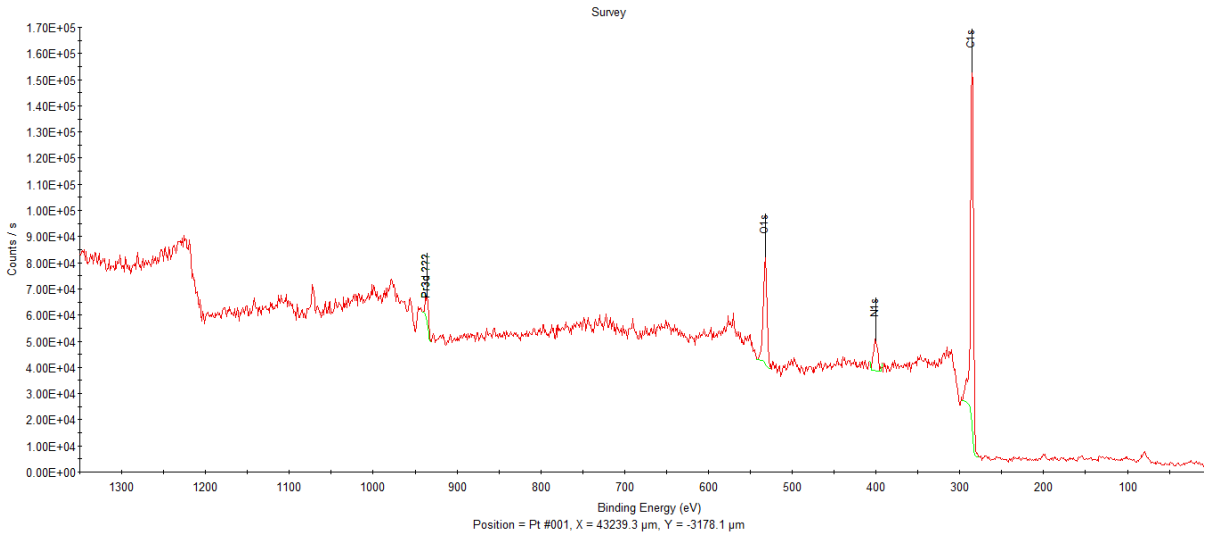

Figure C3: Survey Scan of N-MWCNT after 1hr grinding

a)

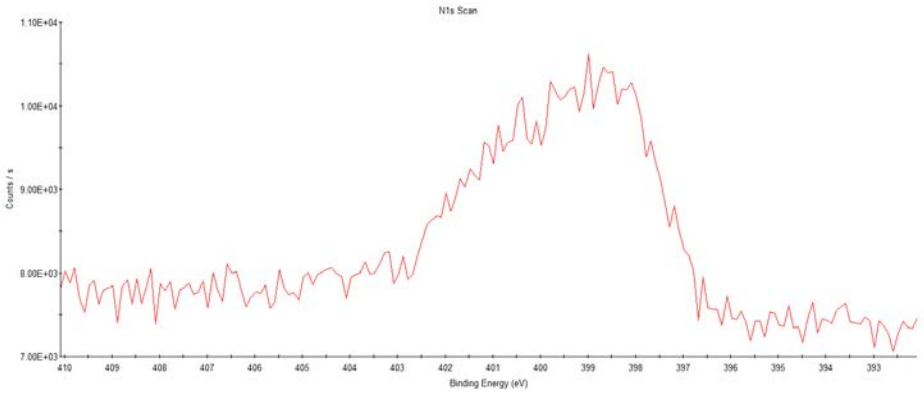

b)

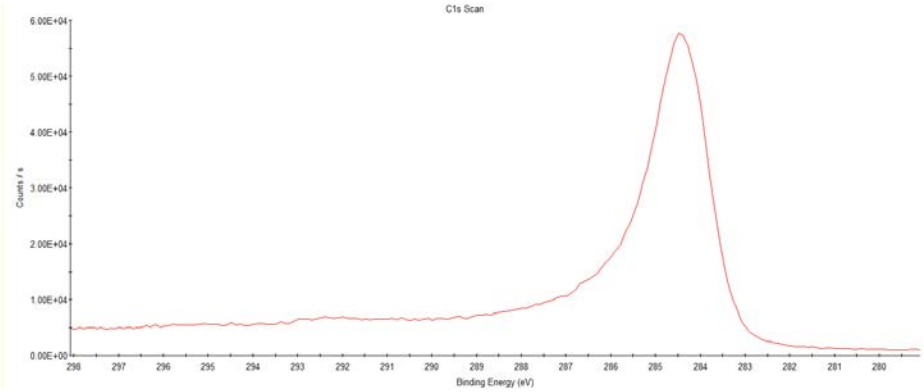

c)

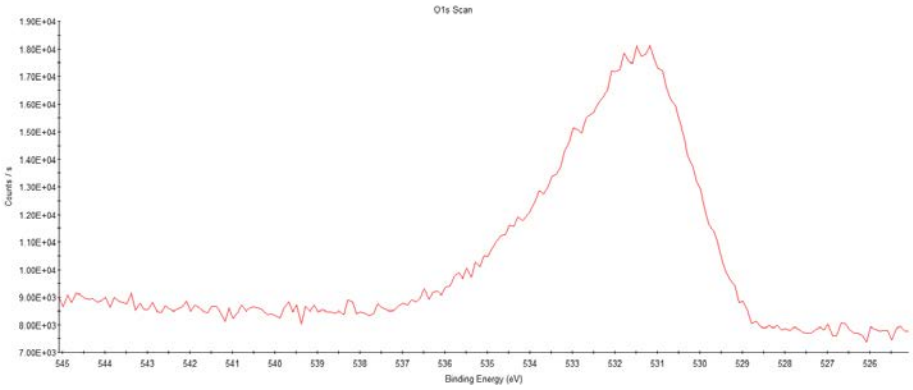

Figure C4: High resolution XPS spectra of N-MWCNTs after 1hr milling showing: a) nitrogen peaks, b) carbon peaks, and c) oxygen peaks. Atomic % values were obtained by integration of the peaks.

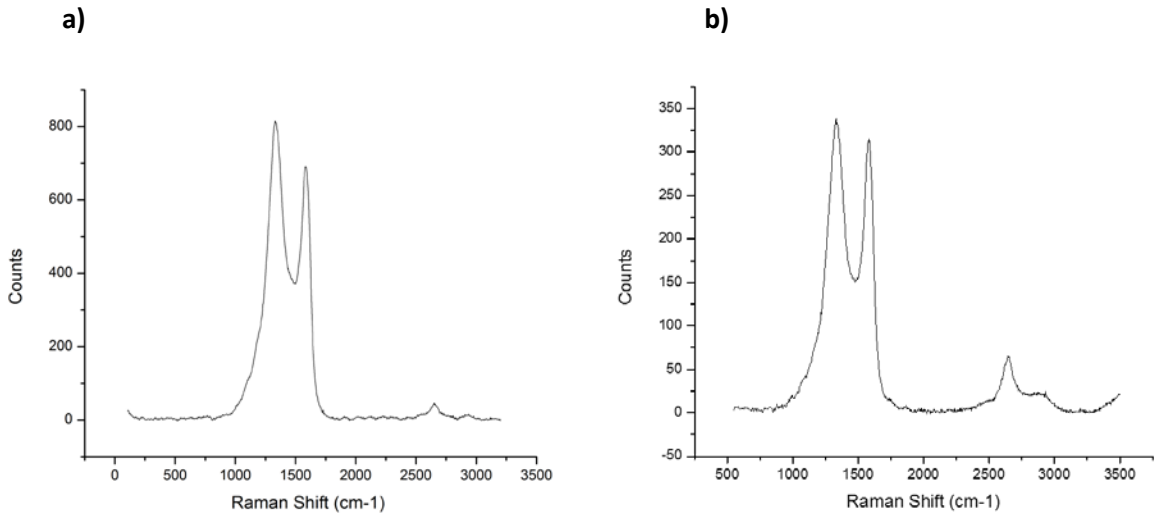

Figure C5: Averaged Raman spectra of base-piranha/HCl treated N-MWCNTs a) before and b) after 1hr grinding with mortar and pestle.

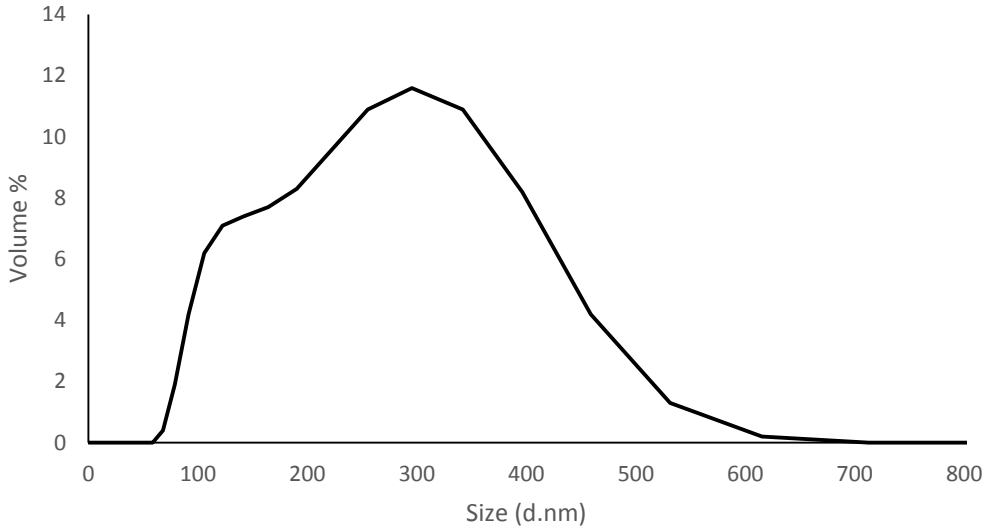

Figure C6: DLS measurement of supernatant containing NCNCs suspended in aqueous 0.1 wt% SDS.

Bibliography

1. Radushkevich, L. O strukture ugleroda, obrazujucegosja pri termiceskom razlozenii okisi ugleroda na zeleznom kontakte. *Zurn Fisic Chim* **26,** 88–95 (1952).

2. Iijima, S. Helical microtubules of graphitic carbon. *Nature* **354,** 56–58 (1991).

3. Wang, X. *et al.* Fabrication of ultralong and electrically uniform single-walled carbon nanotubes on clean substrates. *Nano Lett.* **9,** 3137–41 (2009).

4. Peng, B. *et al.* Measurements of near-ultimate strength for multiwalled carbon nanotubes and irradiation-induced crosslinking improvements. *Nat. Nanotechnol.* **3,** 626–631 (2008).

5. Hong, S. & Myung, S. Nanotube electronics: a flexible approach to mobility. *Nat. Nanotechnol.* **2,** 207–208 (2007).

6. Geier, M. L. *et al.* Solution-processed carbon nanotube thin-film complementary static random access memory. *Nat Nano* **10,** 944–948 (2015).

7. Zhang, M., Atkinson, K. R. & Baughman, R. H. Multifunctional Carbon Nanotube Yarns by Downsizing an Ancient Technology. *Sci.* **306 ,** 1358–1361 (2004).

8. Giraldo, J. P. *et al.* Plant nanobionics approach to augment photosynthesis and biochemical sensing. *Nat Mater* **13,** 400–408 (2014).

9. Lam, C., James, J. T., McCluskey, R., Arepalli, S. & Hunter, R. L. A Review of Carbon Nanotube Toxicity and Assessment of Potential Occupational and Environmental Health Risks. *Crit. Rev. Toxicol.* **36,** 189–217 (2006).

10. Geim, A. K. & Novoselov, K. S. The rise of graphene. *Nat. Mater.* **6,** 183–191 (2007).

11. Novoselov, K. S. *et al.* Electric field effect in atomically thin carbon films. *Science* **306,** 666–669 (2004).

12. Saito, R., Hofmann, M., Dresselhaus, G., Jorio, a. & Dresselhaus, M. S. Raman spectroscopy of graphene and carbon nanotubes. *Adv. Phys.* **60,** 413–550 (2011).

13. Samsonidze, G. G. *et al.* The Concept of Cutting Lines in Carbon Nanotube Science. *J. Nanosci. Nanotechnol.* **3,** 431–458 (2003).

14. Wilder, J. W. G., Venema, L. C., Rinzler, A. G., Smalley, R. E. & Dekker, C. Electronic structure of atomically resolved carbon nanotubes. *Nature* **391,** 59–62 (1998).

15. Andrews, R., Jacques, D., Qian, D. & Rantell, T. Multiwall Carbon Nanotubes: Synthesis and Application. *Acc. Chem. Res.* **35,** 1008–1017 (2002).

16. Zhang, X., Sreekumar, T. V, Liu, T. & Kumar, S. Properties and Structure of Nitric Acid Oxidized Single Wall Carbon Nanotube Films. *J. Phys. Chem. B* **108,** 16435–16440 (2004).

17. Zhao, Y., Tang, Y., Chen, Y. & Star, A. Corking carbon nanotube cups with gold nanoparticles. *ACS Nano* **6,** 6912–6921 (2012).

18. Jang, J. W., Lee, C. E., Lyu, S. C., Lee, T. J. & Lee, C. J. Structural study of nitrogen-doping effects in bamboo-shaped multiwalled carbon nanotubes. *Appl. Phys. Lett.* **84,** 2877 (2004).

19. Kurt, R. & Karimi, A. Influence of nitrogen on the growth mechanism of decorated C:N nanotubes. *Chem. Phys. Chem* **6,** 388–392 (2001).

20. Tchoul, M. N., Ford, W. T., Lolli, G. & Resasco, D. E. Effect of Mild Nitric Acid Oxidation on Dispersability , Size , and Structure of Single-Walled Carbon Nanotubes. *Chem. Mater.* **19,** 5765–5772 (2007).

21. Allen, B. L. *et al.* Biodegradation of single-walled carbon nanotubes through enzymatic catalysis. *Nano Lett.* **8,** 3899–903 (2008).

22. Scott, C. D., Arepalli, S., Nikolaev, P. & Smalley, R. E. Growth mechanisms for single-wall carbon nanotubes in a laser-ablation process. *Appl. Phys. A Mater. Sci. Process.* **72,** 573–580 (2001).

23. Kong, J., Cassell, A. M. & Dai, H. Chemical vapor deposition of methane for single-walled carbon nanotubes. *Chem. Phys. Lett.* **292,** 567–574 (1998).

24. Rafique, M. M. A. & Iqbal, J. Production of Carbon Nanotubes by Different Routes — A Review. *J. Encapsulation Adsorpt. Sci.* **1,** 29–34 (2011).

25. Journet, C., Maser, W. K., Bernier, P. & Loiseau, a. Large-scale production of single-walled carbon nanotubes by the electric-arc technique. *Nature* **388,** 20–22 (1997).

26. Keidar, M. Factors affecting synthesis of single wall carbon nanotubes in arc discharge. *J. Phys. D-Applied Phys.* **40,** 2388–2393 (2007).

27. Harris, P. Carbon nanotube science: synthesis, properties and applications. *Boards* (2009). at <http://www.lavoisier.fr/livre/notice.asp?id=OA3WRSA3S6AOWO>

28. Bachilo, S. M. *et al.* Narrow (n,m)-distribution of single-walled carbon nanotubes grown using a solid supported catalyst. *J. Am. Chem. Soc.* **125,** 11186–11187 (2003).

29. Bronikowski, M. J., Willis, P. a., Colbert, D. T., Smith, K. a. & Smalley, R. E. Gas-phase production of carbon single-walled nanotubes from carbon monoxide via the HiPco process: A parametric study. *J. Vac. Sci. Technol. A Vacuum, Surfaces, Film.* **19,** 1800 (2001).

30. Lee, C. J. & Park, J. Growth model of bamboo-shaped carbon nanotubes by thermal chemical vapor deposition. *Appl. Phys. Lett.* **77,** 3397 (2000).

31. Mak, K. F., Ju, L., Wang, F. & Heinz, T. F. Optical spectroscopy of graphene: From the far infrared to the ultraviolet. *Solid State Commun.* **152,** 1341–1349 (2012).

32. Reich, S., Thomsen, C. & Maultzsch, J. *Carbon Nanotubes. Basis Concepts and Physical Properties*. *Angewandte Chemie International Edition* **43,** (2004).

33. Berciaud, S., Cognet, L., Poulin, P., Weisman, R. B. & Lounis, B. Absorption spectroscopy of individual single-walled carbon nanotubes. *Nano Lett.* **7,** 1203–1207 (2007).

34. Harris, D and Bertolucci, M. Symmetry and spectroscopy; an introduction to vibrational and electronic spectroscopy. *Journal of Molecular Structure* **62,** 301 (1980).

35. Fantini, C. *et al.* Optical transition energies for carbon nanotubes from resonant raman spectroscopy: Environment and temperature effects. *Phys. Rev. Lett.* **93,** 1–4 (2004).

36. Cançado, L. G. *et al.* Quantifying defects in graphene via Raman spectroscopy at different excitation energies. *Nano Lett.* **11,** 3190–3196 (2011).

37. Ferrari, A. C. Raman spectroscopy of graphene and graphite: Disorder, electron–phonon coupling, doping and nonadiabatic effects. *Solid State Commun.* **143,** 47–57 (2007).

38. Fultz, B. & Howe, J. M. *Transmission electron microscopy and diffractometry of materials*. *Transmission Electron Microscopy and Diffractometry of Materials* (2008). doi:10.1007/978-3-540-73886-2

39. Williams, D. B. & Carter, C. B. *Transmission Electron Microscopy: A Textbook for Materials Science*. *Materials Science* **V1-V4,** (2009).

40. Di Carlo, E. *et al.* The intriguing role of polymorphonuclear neutrophils in antitumor reactions. *Blood* **97,** 339–345 (2001).

41. Inoguchi, T. Protein Kinase C-Dependent Increase in Reactive Oxygen Species (ROS) Production in Vascular Tissues of Diabetes: Role of Vascular NAD(P)H Oxidase. *J. Am. Soc. Nephrol.* **14,** 227S–232 (2003).

42. Kinkade, J. *et al.* No Differential distribution of distinct forms of myeloperoxidase in different azurophilic granule subpopulations from human neutrophils. *Biochem. Biophys. Res. Commun.* **114,** 296–303 (1983).

43. Davies, M. J. Myeloperoxidase-derived oxidation: mechanisms of biological damage and its prevention. *J. Clin. Biochem. Nutr.* **48,** 8–19 (2011).

44. Kagan, V. E. *et al.* Carbon nanotubes degraded by neutrophil myeloperoxidase induce less pulmonary inflammation. *Nat. Nanotechnol.* **5,** 354–359 (2010).

45. Kotchey, G. P., Gaugler, J. A., Kapralov, A. A., Kagan, V. E. & Star, A. Effect of antioxidants on enzyme-catalysed biodegradation of carbon nanotubes. *J. Mater. Chem. B* **1,** 302–309 (2013).

46. Panasenko, O. M. *et al.* Generation of free radicals during decomposition of hydroperoxide in the presence of myeloperoxidase or activated neutrophils. *Biochem. Biokhimiia* **70,** 998–1004 (2005).

47. Lardinois, O. EPR Spin-Trapping of a Myeloperoxidase Protein Radical. *Biochem. Biophys. Res. Commun.* **270,** 199–202 (2000).

48. Kim, Y. a. *et al.* Effect of ball milling on morphology of cup-stacked carbon nanotubes. *Chem. Phys. Lett.* **355,** 279–284 (2002).

49. Al, W. E. T. Anomalously Fast Di ff usion of Targeted Carbon Nanotubes in Cellular Spheroids. 8231–8238 (2015).

50. Shvedova, A. a *et al.* Unusual inflammatory and fibrogenic pulmonary responses to single-walled carbon nanotubes in mice. *Am. J. Physiol. Lung Cell. Mol. Physiol.* **289,** L698–L708 (2005).

51. Poland, C. A. *et al.* Carbon nanotubes introduced into the abdominal cavity of mice show asbestos-like pathogenicity in a pilot study. *Nat Nano* **3,** 423–428 (2008).

52. Brown, D. M. *et al.* An in vitro study of the potential of carbon nanotubes and nanofibres to induce inflammatory mediators and frustrated phagocytosis. *Carbon N. Y.* **45,** 1743–1756 (2007).

53. Møller, P. *et al.* Role of oxidative stress in carbon nanotube-generated health effects. *Arch. Toxicol.* **88,** 1939–1964 (2014).

54. Chen, J. *et al.* Dissolution of Full-Length Single-Walled Carbon Nanotubes. *J. Phys. Chem. B* **105,** 2525–2528 (2001).

55. Sarkar, S., Gurjarpadhye, A. A., Rylander, C. G. & Nichole Rylander, M. Optical properties of breast tumor phantoms containing carbon nanotubes and nanohorns. *J. Biomed. Opt.* **16,** 051304 (2011).

56. Kotchey, G. P. *et al.* A natural vanishing act: The enzyme-catalyzed degradation of carbon nanomaterials. *Acc. Chem. Res.* **45,** 1770–1781 (2012).

57. Gao, W. & Song, J. F. Towards surface acid-base property of the carboxylic multi-walled carbon nanotubes by zero current potentiometry. *Electrochem. commun.* **11,** 1285–1288 (2009).

58. Batrakova, E. V *et al.* A macrophage-nanozyme delivery system for Parkinson's disease. *Bioconjug. Chem.* **18,** 1498–1506 (2007).

59. Zhang, J. *et al.* Effect of Chemical Oxidation on the Structure of Single-Walled Carbon Nanotubes. *J. Phys. Chem. B* **107,** 3712–3718 (2003).

60. Zhang, J. *et al.* Reduction of graphene oxide via L-ascorbic acid. *Chem. Commun. (Camb).* **46,** 1112–1114 (2010).

61. Pham, T. A., Kim, J. S., Kim, J. S. & Jeong, Y. T. One-step reduction of graphene oxide with l-glutathione. *Colloids Surfaces A Physicochem. Eng. Asp.* **384,** 543–548 (2011).

62. Borsook, H. & Keighley, G. Oxidation-reduction potential of ascorbic acid (Vitamin C). *Proc. Natl. Acad. Sci. U. S. A.* **19,** 875–878 (1933).

63. Kagan, V. E. *et al.* Direct evidence for recycling of myeloperoxidase-catalyzed phenoxyl radicals of a vitamin E homologue, 2,2,5,7,8-pentamethyl-6-hydroxy chromane, by ascorbate/dihydrolipoate in living HL-60 cells. *Biochim. Biophys. Acta - Gen. Subj.* **1620,** 72–84 (2003).

64. Borisenko, G. G. *et al.* Glutathione propagates oxidative stress triggered by myeloperoxidase in HL-60 cells. Evidence for glutathionyl radical-induced peroxidation of phospholipids and cytotoxicity. *J Biol Chem* **279,** 23453–23462 (2004).

65. Finley, J. W., Wheeler, E. L. & Witt, S. C. Oxidation of glutathione by hydrogen peroxide and other oxidizing agents. *J. Agric. Food Chem.* **29,** 404–407 (1981).

66. Bhattacharya, K. *et al.* Enzymatic 'stripping' and degradation of PEGylated carbon nanotubes. *Nanoscale* **6,** 14686–90 (2014).

67. Delogu, L. G. *et al.* Carbon nanotube-based nanocarriers: the importance of keeping it clean. *J Nanosci Nanotechnol* **10,** 5293–5301 (2010).

68. Kotchey, G. P. *et al.* The enzymatic oxidation of graphene oxide. *ACS Nano* **5,** 2098–2108 (2011).

69. Russier, J. *et al.* Oxidative biodegradation of single- and multi-walled carbon nanotubes. *Nanoscale* **3,** 893–896 (2011).

70. Shvedova, A. A. *et al.* Impaired clearance and enhanced pulmonary inflammatory/fibrotic response to carbon nanotubes in myeloperoxidase-deficient mice. *PLoS One* **7,** e30923 (2012).

71. Andón, F. T. *et al.* Carbon nanotubes: biodegradation of single-walled carbon nanotubes by eosinophil peroxidase (small 16/2013). *Small* **9,** 2720 (2013).

72. Vlasova, I. I. *et al.* PEGylated single-walled carbon nanotubes activate neutrophils to increase production of hypochlorous acid, the oxidant capable of degrading nanotubes. *Toxicol. Appl. Pharmacol.* **264,** 131–142 (2012).

73. Liu C-H, Zhang H-L. Chemical approaches towards single-species single-walled carbon nanotubes. *Nanoscale*. **2**, 1901-191 (2010).

74. Ando Y, Zhao X, Sugai T, Kumar M. Growing carbon nanotubes. *Mater Today*. **7**, 22-29 (2004)

75. http://www.hk-phy.org/atomic_world/tem/tem02_e.html (accessed 11/6/15)

76. Fiedler TJ. X-ray Crystal Structure and Characterization of Halide-binding Sites of Human Myeloperoxidase at 1.8 A Resolution. *J Biol Chem*. **16**, 11964-11971 (2000)

77. Bhattacharya K, Sacchetti C, El-Sayed R, et al. Enzymatic "stripping" and degradation of PEGylated carbon nanotubes. *Nanoscale*. **6**, 14686-14690 (2014)

78. Datsyuk V, Kalyva M, Papagelis K, et al. Chemical oxidation of multiwalled carbon nanotubes. *Carbon*. **46**, 833-840 (2008)

79. Jeon I-Y, Choi H-J, Jung S-M, et al. Large-scale production of edge-selectively functionalized graphene nanoplatelets via ball milling and their use as metal-free electrocatalysts for oxygen reduction reaction. *J Am Chem Soc*. **135,** 1386-1393 (2013)

80. Jiang L, Gao L, Sun J. Production of aqueous colloidal dispersions of carbon nanotubes. *J Colloid Interface Sci*. **260**, 89-94 (2003)

81. Castro Neto AH., Peres NMR., Novoselov KS., Geim AK., Guinea F. The electronic properties of graphene. *Rev Mod Phys*.**81**,109-162 (2009)

82. Jorio a., Pimenta M a., Souza Filho a. G, Saito R, Dresselhaus G, Dresselhaus MS. Characterizing carbon nanotube samples with resonance Raman scattering. *New J Phys*. **5**, 1-17 (2003)